Main Manuscript for

Optochemical profiling of NMDA receptor molecular diversity at synaptic and extrasynaptic sites

Antoine Sicard[1], Meilin Tian[1], Zakaria Mostefai[1], Sophie Shi[1], Cécile Cardoso[1], Joseph Zamith[1], Isabelle McCort-Tranchepain[2], Cécile Charrier[1], Pierre Paoletti[1,*] and Laetitia Mony[1,*]

[1]Institut de Biologie de l'Ecole Normale Supérieure (IBENS)
Ecole Normale Supérieure, Université PSL, CNRS, INSERM
46 rue d'Ulm, 75005 Paris, France

[2]Université Paris Cité, Laboratoire de Chimie et Biochimie Pharmacologiques et Toxicologiques, CNRS UMR8601, 75006 Paris, France

*co-senior and co-corresponding authors: laetitia.mony@ens.psl.eu; pierre.paoletti@ens.psl.eu

Keywords

NMDA receptors, optopharmacology, synapse, glutamate, neuropharmacology

This pdf file includes:

Main Text
Figures 1 to 6
Extended Data Figures 1 to 10

Inventory of Supplementary Information

Extended Data Fig. 1-10 (this pdf file).

Supplementary Information (Separate pdf file): Supplementary Fig. 1; Supplementary Tables 1-5; and Supplementary Notes 1-3.

Source data (Separate .xlsx file)

Abstract

Neurotransmitter receptors are the linchpin of neuronal communication. These receptors often form large multimeric complexes that differ in their subunit composition, distribution and signaling properties. Studying neurotransmitter receptors in native tissues with subunit stoichiometry resolution remains challenging. This is the case of NMDA receptors (NMDARs), a class of glutamate-gated ion channels playing essential roles in brain development and plasticity. These receptors co-exist as multiple subtypes, with GluN1/GluN2A (GluN2A diheteromers), GluN1/GluN2B (GluN2B diheteromers) and GluN1/2A/2B (GluN2A/2B triheteromers) receptors prevailing. Here, we designed a photochemical tool (Opto2B) enabling specific and reversible modulation of GluN2B diheteromers (while leaving other receptor subtypes unaffected). Using Opto2B, we established the differential contribution of GluN2B diheteromers to synaptic and extrasynaptic NMDAR pools, clarifying decades of controversial research. In particular, we show that in adult CA1 pyramidal cells, GluN2A-receptors predominate in both pools, with no preferential contribution of GluN2B diheteromers to extrasynaptic currents. Our study paves the way for interrogating NMDAR signaling diversity with unprecedented molecular and spatio-temporal resolution.

Introduction

With their ability to convert a chemical message – the presence of the neurotransmitter – into an electrical signal – a change in membrane potential – neurotransmitter receptors are the linchpin of neuronal communication[1]. They also constitute therapeutic targets of prime importance against neurological and psychiatric disorders[2,3]. Neurotransmitter receptors assemble as large macromolecular complexes formed by the association of multiple subunits, usually encoded by large multigenic families. The combinatorial association of constitutive subunits into functional receptors generates a vast diversity of receptor subtypes differing in their molecular composition, localization and functional properties. For instance, $GABA_A$ receptors, which mediate the bulk of inhibitory neurotransmission, associate into pentamers from no less than 19 different subunits giving rise to tens of different $GABA_A$ receptor subtypes in the CNS[4–6]. Similarly, ionotropic glutamate receptors (iGluRs), which mediate the bulk of excitatory neurotransmission, assemble as tetramers from a repertoire of several different subunits resulting into a wide variety of receptor subtypes[7–9]. Individual neurons or synapses may assemble distinct receptors subtypes across spatial locations, developmental stages, and physiological or disease states. There is little doubt that this large variety allows specific receptor subtype to engage into distinct neuronal function. This diversity also holds strong promise for next generation therapeutics through the development of target-specific precision drugs more efficient and better tolerated[2,10]. Nevertheless, we currently lack a clear understanding of the physiological and pathological relevance of the large plurality of neurotransmitter receptor subtypes. Current methodologies based on pharmacology and genetic modifications, although powerful, usually have limitations in terms of molecular specificity and spatiotemporal resolution. Therefore, new strategies are required to better discriminate between receptor subtypes and dissect their distribution and associated signaling pathways.

By combining the power of light, pharmacology and genetics, optogenetic pharmacology offers means to overcome some of these limitations[11–15]. This approach consists in tethering a photoswitchable ligand to a desired receptor subunit. Upon illumination with different wavelengths, the ligand can reach its binding site on the receptor target, or undock from it, resulting in pharmacological modulation of the receptor activity. Optogenetic pharmacology affords exquisite molecular and spatiotemporal resolution, as well as on-demand reversibility[11,13–15].

NMDA receptors (NMDARs), a subfamily of iGluRs, play essential roles in brain development and function[16]. Normal NMDAR signaling controls synaptic plasticity, a cellular substrate of learning and memory. Conversely, abnormal NMDAR function is deleterious causing neuronal injury, cognitive deficits and maladaptive behaviors[16–18]. At the molecular

level, NMDARs are obligatory hetero-tetramers containing two GluN1 subunits and two GluN2 or GluN3 subunits of which there are six versions (GluN2A-2D and GluN3A-B). NMDARs can assemble as diheteromers (with two identical copies of GluN2 or GluN3 subunits) or triheteromers (with two different copies of GluN2 or GluN3 subunits) that co-exist in native tissue, with over ten receptor subtypes identified to date[7,16,19,20]. In the adult forebrain, the GluN2A diheteromers (GluN1/GluN2A), GluN2B diheteromers (GluN1/GluN2B) and GluN2A/GluN2B triheteromers (GluN1/GluN2A/GluN2B) predominate, at mixtures that differ according to cell type, brain region and developmental stage[7,16,20,21]. The GluN2A to GluN2B subunit ratio has been shown to be an essential parameter controlling key neural processes, such as critical periods, bidirectional synaptic plasticity as well as excitotoxic damage[16,22–24]. Yet the respective contribution of GluN2A and GluN2B diheteromers in respect to GluN2A/GluN2B triheteromers in these processes remains controversial. Moreover, the subcellular distribution of these various receptor subtypes, i.e. their distribution between synaptic and extrasynaptic compartments, is also contentious. Genetic manipulation of GluN2A or GluN2B subunits indifferently affects diheteromers and triheteromers. Similarly, available pharmacological agents, such as the 'GluN2A selective' inhibitors zinc and TCN-201, or the 'GluN2B selective' inhibitor ifenprodil (and derivatives), poorly discriminate between their respective diheteromers and triheteromers[20,25–27]. These inherent limitations hamper drawing unambiguous conclusions.

In this work, using optogenetic pharmacology, we designed a new photoswitchable tool targeting NMDARs with subunit stoichiometry resolution. This tool (coined 'Opto2B') allows specific and reversible manipulation of GluN2B diheteromers in complete independence of GluN2A/GluN2B triheteromers (and GluN2A diheteromers). Because Opto2B is based on an allosteric, rather than orthosteric (i.e. targeting the agonist binding sites), photoswitchable ligand, it also minimally interferes with the normal pattern of receptor activation, thus preserving endogenous signaling. Using opto2B, we defined the contribution to hippocampal CA1 NMDA currents of GluN2B diheteromers relative to GluN2A-containing receptors (GluN2A diheteromers and GluN2A/GluN2B triheteromers), both at extrasynaptic and synaptic sites and during brain development up to adulthood. Our study reveals that, early on in postnatal development, GluN2A subunits are excluded from extrasynaptic sites but incorporate readily in synaptic NMDARs, while in adult CA1 pyramidal cells, GluN2B diheteromers are expressed at low levels at synaptic but also extrasynaptic sites.

116 # Results

117 **Design of photocontrollable GluN2B-NMDARs using optogenetic pharmacology**

118 GluN2B-NMDARs are selectively potentiated by polyamines (spermine and spermidine), a
119 class of positively-charged compounds binding at the interface between the lower lobes of
120 GluN1 and GluN2B NTDs[2,28,29]. Polyamines promote GluN1 and GluN2B NTD lower lobe
121 apposition, a motion coupled to a downstream rolling motion between the two GluN1/GluN2B
122 ABD dimers, which in turn leads to an increase in the receptor channel activity[28,30–32]
123 (Figure 1a). We decided to target this allosteric site to modulate GluN2B-NMDARs with light.
124 To this aim, we designed a photoswitchable spermine derivative called MASp (for Maleimide-
125 Azobenzene-Spermine), a tri-partite ligand composed of (Fig. 1b and Supplementary
126 Note 1): (i) a cysteine-reactive maleimide moiety allowing covalent attachment to a cysteine;
127 (ii) an azobenzene group (the photoswitch), which can reversibly alternate between an
128 extended *trans* and a bent *cis* configuration depending on the illumination wavelength; and
129 (iii) a spermine moiety (the ligand), acting as the pharmacological head-group. MASp was
130 best switched from *trans* to *cis* by 365 nm light illumination, and from *cis* to *trans* by
131 wavelengths of ~500 nm, as revealed by UV-visible spectroscopy (Extended Data Fig. 1a).
132 Hence, thereafter, we used the wavelength of 365 nm to optimally photoswitch MASp from
133 *trans* to *cis*, and wavelengths from 490 to 530 nm to induce *cis* to *trans* conversion. Further
134 characterization of MASp physicochemistry revealed efficient and reversible photoswitching
135 as well as bistability, properties highly suitable for biological use (Extended Data Fig. 1b,c
136 and Supplementary Note 1- Spectra S1g,h).

137 We next searched for a MASp attachment site on the GluN2B subunit for optimal
138 photomodulation. Ideally, MASp tethered to the GluN2B subunit should be inert in one
139 configuration (*cis* or *trans*), while inducing receptor potentiation in the other configuration
140 (Fig. 1a). To identify potential MASp attachment sites, we performed individual cysteine
141 scanning mutagenesis targeting solvent-accessible residues of the GluN2B α5-β7 region
142 proposed to participate in the spermine binding site[28,31,32] (Fig. 1c,d). Screening was
143 performed in Xenopus oocytes expressing GluN1/GluN2B receptors with various cysteine
144 mutants in the GluN2B subunit, and labeled with MASp (see Methods and Extended Data
145 Fig. 1d). Because spermine potentiation displays strong pH-dependence[28,33], functional
146 screening was performed at an acidic pH (pH 6.5) to maximize chances of observing
147 photomodulation.

148 We first tested potential background effects of MASp labeling on wild-type (WT)
149 GluN1/GluN2B receptors. Currents from WT GluN2B diheteromers labeled with MASp were
150 not affected by 365 or 490 nm illumination (Fig. 1e). However, MASp labeling by itself

151 induced a marked (~3-fold) increase in receptor channel open probability (Po), as assessed
152 by measuring the kinetics of current inhibition by MK-801, an NMDAR open channel
153 blocker[34–38] (Extended Data Fig. 1e,f). This effect was due to conjugation of MASp to the
154 endogenous cysteine C395, located in the short linker segment between the NTD and the
155 ABD of the GluN2B subunit (Extended Data Fig. 1e). Indeed, MASp-induced Po increase
156 was fully abolished in mutant GluN1/GluN2B-C395S receptors, in which C395 was rendered
157 non-reactive (Extended Data Fig. 1g,h). To avoid effect of MASp on WT GluN2B-receptors,
158 we subsequently used receptors containing the background mutation GluN2B-C395S (noted
159 hereafter GluN2B*). Importantly, the C395S mutation by itself had no significant impact on
160 GluN2B-receptor channel Po (Extended Data Fig. 1h).

161 Among the 23 labeling positions tested, significant (>30%) photomodulation was
162 observed for 8 of them (Fig. 1d). Most of these positions were clustered on the GluN2B α5
163 helix, which occupies a central position at the dimer interface of GluN1/GluN2B NTD dimer in
164 its active state[31] (Fig. 1c,d). Interestingly, at 3 positions located at the 'top' (N-terminal end) of
165 the α5 helix, currents under 365 nm light were smaller than under 490 nm light (Fig. 1c,d, red
166 squares), while at downstream positions the opposite was observed (currents under 365 nm
167 light stronger than under 490 nm light; Fig. 1c,d green squares). The strongest
168 photomodulation ratios were obtained for positions GluN2B-Q180C and -R187C, with 2.5-
169 fold UV-induced current inhibition ($I_{365\ nm}/I_{490\ nm}$ = 0.39 ± 0.02, n = 27) and close to 4-fold UV-
170 induced current potentiation ($I_{365\ nm}/I_{490\ nm}$ = 3.5 ± 0.2, n = 32) (Fig. 1d,e and Supplementary
171 Table 1), respectively. As observed with other azobenzene-based photoswitchable ligands[39–
172 43], the photomodulation showed high reversibility and reproducibility, allowing multiple cycles
173 of illumination without fatigability (Fig. 1e). These experiments also confirm that *cis*-MASp is
174 kinetically stable, since no current relaxation was observed upon interruption of the UV
175 illumination (see end of illumination cycle in Fig. 1e). The opposite light effects observed at
176 the Q180C and R187C positions are due to opposing effects of MASp *cis* and *trans*
177 configurations. Indeed, at the Q180C position, MASp acts as a *trans*-on photoswitch: it
178 constitutively occupies the spermine binding-site in its *trans* form (under 490 nm light, as
179 revealed by the ~3 fold Po increase after MASp labeling), hence potentiating receptor activity
180 (Fig. 1e and Extended Data Fig. 2a). Conversion by UV light to its *cis* isomer withdraws the
181 spermine moiety from its potentiating binding site, allowing the receptor to revert to its basal
182 state (similar Po as the non-labeled receptor). In contrast, MASp conjugated to GluN2B-
183 R187C acts as a *cis*-on photoswitch: there is no effect on receptor channel Po under 490 nm
184 light, while Po is increased by ~3.5-fold under UV-light (*cis* configuration, Fig. 1e and
185 Extended Data Fig. 2b). We thus have on-hand two complementary optopharmacological

186 tools for remote and reversible photocontrol of GluN2B-NMDARs with either UV (R187C) or
187 green light (Q180C) illumination.

188 We then assessed the extent of MASp photomodulation of GluN1/GluN2B*-Q180C
189 and GluN1/GluN2B*-R187C receptors at physiological pH (pH 7.3). Similarly to what was
190 observed for spermine potentiation of GluN2B-NMDARs[28,33], photomodulation at pH 7.3 was
191 lower than at acidic pH (Extended Data Fig. 2c,d). The UV-induced current inhibition of
192 MASp-labeled GluN1/GluN2B*-Q180C receptors dropped from ~2.5-fold at pH 6.5 to ~1.2-
193 fold at pH 7.3 ($I_{365\ nm}/I_{490\ nm}$ = 0.84 ± 0.08, n = 13; Extended Data Fig. 2c,d and
194 Supplementary Table 1). Photomodulation at pH 7.3 was also lower for MASp-labeled
195 GluN1/GluN2B*-R187C receptors, although it remained robust, with ~2-fold photomodulation
196 of receptor activity ($I_{365\ nm}/I_{490\ nm}$ = 1.97 ± 0.17, n = 21; Extended Data Fig. 2c,d). Finally, we
197 evaluated the functional impact of the GluN2B-Q180C and -R187C mutations (together with
198 the C395S background mutation) on receptor activity, as well as on receptor sensitivity to
199 agonists (glutamate and glycine) and endogenous allosteric modulators spermine and
200 protons[44,45]. The Q180C mutation itself (- MASp condition in Extended Data Fig. 2e-i and
201 Supplementary Table 2) had no significant effect on any of the above parameters. MASp
202 binding to Q180C in its inactive (*cis*) form (+ MASp, UV condition) did not either induce any
203 significant change in receptor function, except a decrease in spermine sensitivity, likely
204 because MASp partially occupies (or hinders) the polyamine site. Functional effects of the
205 R187C mutation and its subsequent labeling with MASp were also mild, although more
206 marked than for Q180C. The R187C mutation by itself induced modest effects on receptor
207 activity (Extended Data Fig. 2e-i and Supplementary Table 2), while conjugation of MASp in
208 its inactive (*trans*) form (490 nm PSS, Extended Data Fig. e-i) did not further perturb receptor
209 function. It even restored spermine and proton sensitivities to WT levels (Extended Data
210 Fig. 2h,i and Supplementary Table 2). Overall, it appears that R187C combines many
211 advantages, including robust *cis*-on photomodulation at physiological pH, making this site
212 particularly attractive for implementation in native tissues (Extended Data Fig. 2j and
213 Supplementary Table 2). Therefore, we focused on receptors containing the GluN2B*-R187C
214 subunit conjugated with MASp (Opto2B tool).

215

216 **Selective photomodulation of GluN2B diheteromers**

217 *In vivo*, NMDARs exist as multiple subtypes that differentially populate brain regions and cell
218 types[16]. To determine the MASp selectivity towards the different NMDAR subtypes, we first
219 verified the effect of MASp labeling on diheteromeric GluN1/GluN2A receptors, an abundant
220 pool of NMDARs in the adult brain. Currents from Xenopus oocytes expressing MASp-

221 treated WT GluN1/GluN2A receptors displayed only modest photomodulation, with a small
222 (8%) UV-induced inhibition ($I_{365\ nm}/I_{490\ nm}$ = 0.92 ± 0.02, n = 22; Fig. 2a,b, and Supplementary
223 Table 1). Moreover, MASp labeling by itself had no significant effect on GluN1/GluN2A
224 receptor channel Po (Fig. 2c). Similarly, MASp-treated GluN1/GluN2C and GluN1/GluN2D
225 receptors displayed no photomodulation (1.02 ± 0.006, n = 5; 1.00 ± 0.008, n = 5
226 respectively; Fig. 2a,b and Supplementary Table 1). This is consistent with the fact that the
227 spermine potentiating NTD site is present on GluN2B-, but not GluN2A-, GluN2C- and
228 GluN2D-NMDARs[28,33,46].

229 Since GluN2A/GluN2B triheteromers are thought to form a sizeable proportion of
230 NMDAR subtypes in the adult forebrain[20], we characterized the photosensitivity of
231 GluN2A/GluN2B*-R187C triheteromers labeled with MASp. For that purpose, we used a
232 previously published approach based on retention signals (hereby named r1 and r2) of
233 $GABA_B$ receptors that allows selective expression of NMDAR triheteromers at the cell
234 surface[27] (see also ref. [25]). No significant photomodulation of MASp-labeled
235 GluN2A/GluN2B*-R187C triheteromers was observed (GluN2A-r1/GluN2B*-R187C-r2;
236 $I_{365\ nm}/I_{490\ nm}$ = 1.01 ± 0.01, n = 17; Fig. 2d,e and Supplementary Table 1). This lack of
237 photosensitivity could not be attributed to the insertion of the retention signals since MASp-
238 tethered GluN2B*-R187C diheteromers expressed using the same retention system
239 displayed strong photomodulation similar to their control counterparts (GluN2B*-R187C-
240 r1/GluN2B*-R187C-r2; $I_{365\ nm}/I_{490\ nm}$ = 3.07 ± 0.22, n = 9; Fig. 2d,e). Finally, GluN2B-NMDARs
241 containing only one copy of the mutant GluN2B*-R187C subunit displayed an intermediate
242 level of photomodulation (GluN2B-r1/GluN2B*-R187C-r2; $I_{365\ nm}/I_{490\ nm}$ = 1.21 ± 0.02, n = 14;
243 Fig. 2d,e). MASp therefore discriminates according to subunit copy number. A single GluN2B
244 subunit is insufficient to endow light sensitivity while strong photocontrol is gained when two
245 photosensitive copies of GluN2B are assembled in the receptor, thus allowing selective
246 modulation of GluN2B diheteromers. In that regard, Opto2B is unique, outperforming
247 currently available subtype-specific pharmacological tools, such as the GluN2B-specific
248 inhibitor ifenprodil, or the GluN2A-specific inhibitor zinc, which all poorly distinguish between
249 diheteromers and triheteromers[20,25–27].

250

251 **Fast on-demand photocontrol of GluN2B diheteromers in mammalian cells**

252 We investigated MASp-induced photomodulation in mammalian cells. Similarly to Xenopus
253 oocytes, MASp-labeled WT GluN2B diheteromers expressed in HEK cells were not
254 photosensitive and WT GluN2A diheteromers displayed only minor UV-induced inhibition
255 (Extended Data Fig. 3a,b). GluN2B*-Q180C diheteromers displayed a small

256 ($I_{365\ nm}/I_{490\ nm}$ = 0.77 ± 0.07, n = 4; Extended Data Fig. 3a,b) photo-inhibition similar to the one
257 observed in Xenopus oocytes at physiological pH (see above). In contrast, currents from
258 MASp-labeled GluN2B*-R187C diheteromers expressed in HEK cells displayed strong and
259 fully reversible UV-induced potentiation at physiological pH ($I_{365\ nm}/I_{525\ nm}$ = 3.2 ± 0.3, n = 18,
260 pH 7.3; Extended Data Fig. 3a,b), thus qualitatively mirroring the results obtained in oocytes.
261 Quantitatively however, the extent of photomodulation (~3-fold) was significantly higher than
262 that observed in oocytes at physiological pH (~2-fold). This difference presumably stems
263 from the spherical nature and opacity of oocytes, while HEK293 cells are transparent and
264 flatter, allowing more efficient and broader photoswitching of expressed GluN2B*-R187C
265 diheteromers. Current potentiation by UV illumination was similar whether light was applied
266 during agonist application (active state) or before agonist application (resting state)
267 (Extended Data Fig. 3c,d). UV illumination by itself had no (or little, see below) effect on the
268 baseline current (recorded in the absence of agonist), as expected from MASp acting as a
269 genuine allosteric ligand, modulating but not directly activating the receptors. Finally, the
270 kinetics of GluN2B*-R187C photoswitching were fast, with time constants of ~60 ms for UV-
271 induced potentiation and of 13 to 450 ms for return to the basal state depending on the
272 illumination conditions (Extended Data Fig. 3f,g and Supplementary Note 2).

273 We finally tested MASp-induced photomodulation in cultured mouse cortical neurons
274 transfected with the GluN2B-R187C* subunit. NMDAR currents from non-fluorescent
275 neurons, which do not express the mutant GluN2B*-R187C subunit, displayed minimal
276 photomodulation ($I_{365\ nm}/I_{525\ nm}$ = 0.968 ± 0.009, n = 9; Extended Data Fig. 4a,b and
277 Supplementary Table 1), consistent with minimal effects of MASp-labeling on native, WT
278 NMDARs. In contrast, UV illumination robustly potentiated currents from GFP-positive
279 neurons expressing the GluN2B*-R187C subunit and labeled with MASp
280 ($I_{365\ nm}/I_{525\ nm}$ = 1.81 ± 0.09, n = 19; Extended Data Fig. 4a,b and Supplementary Table 1).
281 The lower photomodulation ratio observed in neurons compared to HEK cells is likely due to
282 the presence of endogenous GluN2A and GluN2B-NMDARs, which contribute to the NMDAR
283 current but are photo-insensitive. Overall, these experiments demonstrate that the Opto2B
284 tool is transposable to cultured neurons with intact potentiality.

285

286 **Selective photomodulation of synaptic and NMDA tonic currents in brain slices**

287 Motivated by the successful implementation of Opto2B in cultured neurons, we next moved
288 to more native preparations using acute brain slices. As a proof-of-concept, we used cortex-
289 directed *in utero* electroporation of E15.5 mouse embryos to allow the sparse and specific
290 modification of layer II/III cortical pyramidal neurons from the somatosensory cortex in their

291 intact environment (Fig. 3a). This technique furthermore allows monitoring fluorescent (i.e.
292 electroporated) neurons and non-fluorescent (i.e. control) neurons, in the same
293 preparation[47,48]. Similarly to cultured cortical neurons, we restricted the electroporation to the
294 GluN2B*-R187C subunit, not including the GluN1 subunit, to limit NMDAR over-expression.
295 Acute slices were incubated during 30 min in 6.6 μM MASp and then washed before
296 recording (Fig. 3a and see Methods). Synaptic currents were induced by stimulation near the
297 apical dendrite of the patched cortical pyramidal neuron (Fig. 3a).

298 In fluorescent neurons expressing the GluN2B*-R187C subunit and labeled with
299 MASp, UV light induced an increase in NMDA-EPSC amplitude of up to 1.45-fold (in P11-14
300 mice) compared to EPSCs recorded under green light (Fig. 3b,c and Supplementary Table 3,
301 and see Methods and Extended Data Fig. S5a,b for the protocol of light stimulation). As in
302 recombinant systems, this photomodulation was reversible and reproducible, with no sign of
303 photo-fatigue for at least two cycles of UV-green light stimulations (Fig. 3b and Extended
304 Data Fig. 5b). No photomodulation of NMDA-EPSCs was observed in control, non-
305 fluorescent neurons (Fig. 3b; Extended Data Fig. 5b; and Supplementary Table 3). We also
306 detected a significant photomodulation in fluorescent cells from P21-P25 mice (Extended
307 Data Fig. 5c and Supplementary Table 3). We found that MASp labeling by itself had minimal
308 impact on synaptic transmission, as indexed by the absence of modification of the
309 NMDA/AMPA ratio (Extended Data Fig. 5c) and the lack of photomodulation of AMPA-EPSCs
310 (Extended Data Fig. 5e-g). It furthermore had minimal impact on the intrinsic neuronal
311 electrical properties and excitability, (Extended Data Fig. 5h-j). Taken together, these results
312 show that MASp is operational in intact neuronal networks allowing selective manipulation
313 and detection of GluN2B diheteromers with minimal off-target effects.

314 During the course of our recordings, we systematically observed in MASp-treated
315 slices a large (up to several hundreds of pA) and transient increase of the tonic (i.e. holding)
316 current at the onset of the UV illumination pulse (Fig. 3d). UV-induced increase in tonic
317 current occurred in the ~15 ms time-range (Extended Data Fig. 6a,b) but the current relaxed
318 close to basal level with a time constant of ~200 ms despite the continuous presence of UV
319 light (no green light application) (Fig. 3d and Extended Data Fig. 6a,b). However, illumination
320 with green light was necessary to allow subsequent UV-induced potentiation of the tonic
321 current and, similarly to synaptic currents, this process was reproducible over several cycles
322 of illumination without visible photo-fatigue (Extended Data Fig. 6c). This current peak was
323 absent in non-fluorescent neurons (Fig. 3d,e and Extended Data Fig. 6c,d) and was fully
324 abolished by application of 50 μM of the NMDAR-specific antagonist APV (Fig. 3d and
325 Extended Data Fig. 6e). Thus, we can safely conclude that this transient UV-induced current
326 is mediated by light-sensitive GluN2B diheteromers. In principal neurons of the forebrain,

327 extrasynaptic NMDARs contribute to tonic currents by binding ambient glutamate present at
328 low concentrations in the extracellular space[49–53]. Monitoring the large and transient
329 potentiation of NMDA tonic currents should therefore allow us to probe with high sensitivity
330 the presence of GluN2B*-R187C diheteromers at extrasynaptic sites.

331 We hypothesized that the transient nature of the UV-induced potentiation of tonic
332 NMDA currents reflected glutamate dissociation from potentiated receptors. Spermine
333 potentiation of GluN2B diheteromers (but also UV potentiation by MASp, Extended Data
334 Fig. 2e and Supplementary Table 2) is known to come with a slight decrease in the receptor's
335 glutamate sensitivity[54]. Recordings from cultured cortical neurons transfected with GluN2B*-
336 R187C confirmed that MASp photo-potentiation decayed with time when sub-saturating
337 glutamate concentrations were used, while under saturating agonists, UV light yielded
338 sustained, non-desensitizing potentiation (Extended Data Fig. 7a,b). Thus, in brain slices, the
339 low (i.e. non-saturating) glutamate concentrations likely account for the transient nature of
340 UV potentiation of tonic NMDA currents. To confirm this hypothesis, we artificially raised
341 ambient glutamate extracellular concentration in brain slices by perfusing the glutamate
342 transporter inhibitor DL-threo-β-Benzyloxyaspartic acid (TBOA). As expected, application of
343 TBOA resulted in a strong increase of tonic current levels (average ± s.e.m tonic current at
344 +40 mV of 438 ± 101 pA before TBOA *vs* 1469 ± 108 pA after TBOA treatment, n = 8, p-
345 value = 0.008, Wilcoxon matched-pairs signed rank test). Upon subsequent UV-light
346 application, the UV-induced peak did not fully decay, reaching a steady-state current
347 significantly larger than basal levels, and that was reversed by green light ($\Delta_{UV, SS}$ / $\Delta_{UV, peak}$ =
348 0.15 ± 0.02 before TBOA and 0.46 ± 0.08 after TBOA; n = 8; Extended Data Fig. 6f,g). In
349 some cases, the UV potentiation was sustained with minimal decay of the tonic NMDA
350 currents indicating glutamate concentrations following TBOA treatment high enough to
351 saturate the receptors' glutamate binding sites (Extended Data Fig. 6f). By comparing the
352 ratio of steady-state over peak of the UV-induced current increase in absence of TBOA
353 ($\Delta_{UV, SS}$ / $\Delta_{UV, peak}$ = 0.15 ± 0.02, Extended Data Fig. 6g) to the values measured in dissociated
354 neurons (Extended Data Fig. 7b), we estimated the basal glutamate concentration to be in
355 the 30 to100 nM range around cortical pyramidal neurons, consistent with the literature[55–57].
356 Given the low occupancy of extrasynaptic NMDARs by tonic glutamate at these
357 concentrations and the large peak current elicited by UV illumination, our findings indicate
358 that extrasynaptic sites express a high amount of GluN2B diheteromers. Hence, the very fast
359 control of GluN2B diheteromers by light allows separation of the two opposite effects of
360 polyamine modulation: increase of channel Po and decrease of glutamate potency[28,54]. As
361 MASp is converted from *trans* to *cis* by UV light, it reaches its NTD modulatory site leading to
362 an increase of Po in a ~15 ms time range, which corresponds to the peak of UV-induced

363 increase in tonic current. Subsequent UV peak relaxation reflects glutamate dissociation,
364 with much slower kinetics (~200 ms, see above) that are similar to the NMDA EPSC decay
365 kinetics measured from fluorescent neurons (weighted τ_{off} = 198 ± 13 ms, n = 8). In addition,
366 the amount of relaxation makes it possible to estimate the local tonic glutamate concentration
367 around the recorded neuron.

368 Unlike steady-state UV potentiation, peak UV potentiation as assessed on
369 recombinant receptors was largely independent on glutamate concentration, with <10%
370 variation of photomodulation between 0.03 and 100 μM of glutamate (Extended Data Fig. 7c-
371 e and Supplementary Note 3). Measurement of UV-induced potentiation at the peak
372 therefore allows comparison of the proportions of GluN2B diheteromers between neurons
373 and neuronal compartments regardless of their local glutamate environment. Varying
374 concentrations of the co-agonist glycine also had only small effects on the extent of
375 photomodulation measured at the UV peak (Extended Data Fig. 7f-h and Supplementary
376 Note 3). For each individual cell in brain slices, we thus estimated the level of tonic NMDAR
377 current photo-enhancement by measuring the UV-induced peak current and comparing it to
378 the amplitude of basal tonic current mediated by NMDARs deduced from APV inhibition
379 under green light ($I_{365\ nm}$ / $I_{530\ nm}$ on Fig. 3D; and see Methods). Using this approach, we found
380 that UV light induced massive potentiation of tonic NMDARs, >3.5-fold in slices from juvenile
381 (P11-14) mice ($I_{365\ nm}$ / $I_{530\ nm}$ = 3.8 ± 1.3, n = 9; Fig. 3e; Supplementary Table 3, and see also
382 Extended Data Fig. 6h for older ages). These results indicate a strong presence of GluN2B
383 diheteromers at extrasynaptic compartments at young postnatal ages, confirming previous
384 work[51,58]. They also show the potential of our tool to precisely estimate the amount of GluN2B
385 diheteromers at synaptic and extrasynaptic sites relatively to existing pharmacological agents
386 such as ifenprodil or polyamines, whose effects on tonic currents are difficult to interpret due
387 to the glutamate-dependence of their mode of action[54,59].

388

389 **Developmental regulation of endogenous synaptic and extrasynaptic NMDAR**
390 **subtypes in the hippocampus**

391 With its ability to probe the proportion of GluN2B diheteromers at synaptic and extrasynaptic
392 sites, Opto2B appears well suited to dissect the molecular composition of NMDARs across
393 development and subcellular compartments. To avoid overexpression and maintain
394 endogenous levels and patterns of GluN2B-NMDAR expression, we generated a knock-in
395 (KI) mouse containing a mutant GluN2B subunit allowing for MASp attachment and
396 photomodulation (Opto2B mouse). While in Xenopus oocytes (see above and Extended Data
397 Fig. 2) and HEK cells (Extended Data Fig. 8a), neutralizing the endogenous cysteine

398 GluN2B-C395 was required to avoid background effects of MASp, no such undesired effects
399 were observed in cultured cortical neurons (similar large photomodulation between GluN2B*-
400 R187C and GluN2B-R187C receptors, Extended Data Fig. 8b and Supplementary Table 1).
401 This suggests that, in neurons, MASp does not react with GluN2B-C395. Accordingly, to limit
402 the number of introduced mutations, we generated a KI mouse harboring the single GluN2B-
403 R187C mutation (Opto2B mouse, Fig. 4a). Using kinetics measurements and classical
404 pharmacology, we verified that the basal GluN2A/GluN2B subunit ratio at hippocampal CA3-
405 CA1 synapses (synapses of interest, see below) was unaffected in MASp-labeled Opto2B
406 mice compared to unlabeled WT animals (Extended Data Fig. 9a-d), indicating no significant
407 alteration of NMDA synaptic currents and subunit content by the GluN2B-R187C mutation
408 and MASp labeling step.

409 We focused on hippocampal CA1 neurons and CA3-CA1 synapses, which have been
410 extensively studied for their NMDAR receptor content. Adult CA1 neurons express high
411 levels of GluN2A and GluN2B subunits, but little or no GluN2C and GluN2D subunits[60–62].
412 CA1 neurons also display the typical GluN2B to GuN2A 'switch' whereby, following birth,
413 expression of the GluN2A subunit gradually increases, leading to increasing incorporation of
414 GluN2A-containing NMDARs and a proportional decrease in GluN2B-containing
415 receptors[7,16,23]. However, in which proportions GluN2A and GluN2B subunits associate to
416 form GluN2A and GluN2B diheteromers, or GluN2A/2B triheteromers, and how these
417 subtypes segregate between synaptic and extrasynaptic sites remains elusive and subject to
418 controversy[51,58,63–65].

419 To study synaptic NMDARs through development, we prepared acute brain slices
420 from Opto2B mice at different age ranges (P5, P8-P12, P20-P23 or P37-P47), which were
421 labeled with 6.6 μM MASp. NMDA synaptic currents (NMDA-EPSCs) were recorded on
422 patched CA1 pyramidal neurons by stimulating the Schaeffer collaterals, either under UV
423 light, or under green light (Fig. 4B, similar protocol as Extended Data Fig. 5a). UV light
424 induced ~1.4-fold potentiation of NMDA-EPSC peak currents compared to green light at
425 young ages (P5-P12) while no effect of light was observed on MASp-labeled slices from WT
426 animals (at P8-P12, $I_{365\ nm}/I_{530\ nm}$ = 1.41 ± 0.06, n = 20 for Opto2B mice vs 1.02 ± 0.04, n = 10
427 for WT; Fig. 4c,d and Supplementary Table 4). The photomodulation in Opto2B animals
428 decreased progressively with development to reach 1.14-fold around P40, indicative of a
429 progressive decrease in the GluN2B diheteromer contribution to synaptic currents during
430 development (Fig. 4c, left; Fig. 4d, dark-blue bars; and Supplementary Table 4). To gain
431 insights into the origin of this drop in photomodulation, we crossed the Opto2B mouse line
432 with a GluN2A-KO mouse line[66] in order to prevent expression of any GluN2A-NMDARs
433 (including GluN2A diheteromers and GluN2A/GluN2B triheteromers). Compared to Opto2B

434 slices, the photomodulation of NMDA-EPSC peak currents was markedly and systematically
435 higher for Opto2B/GluN2A-KO slices, showing co-existence of GluN2B diheteromers with
436 GluN2A-NMDARs at synaptic sites already at young ages (< P12; Fig. 4c,d and
437 Supplementary Table 4). This difference increased with age (Fig. 4c,d and Supplementary
438 Table 4), consistent with an increasing expression and incorporation of the GluN2A subunit in
439 synaptic NMDARs during postnatal development[7,16,23,67,68]. This result is consistent with the
440 developmental acceleration of NMDA-EPSC decay kinetics in slices from Opto2B mice, an
441 effect absent in Opto2B/GluN2A-KO animals (Extended Data Fig. 9e,f).

442 We next studied the photomodulation of tonic NMDA currents across development on
443 slices from Opto2B and Opto2B/GluN2A-KO animals to estimate the evolution of the
444 proportion of GluN2B diheteromers in extrasynaptic compartments (Fig. 5a,b and Extended
445 Data Fig. 10a). We first verified that no significant photomodulation of tonic NMDA currents
446 was present on MASp-treated slices from WT animals (0.94 ± 0.04, n = 4; Fig. 5b and
447 Extended Data Fig. 10b). At early postnatal ages (before P12), massive, and quantitatively
448 similar, UV potentiation of NMDA tonic currents (>2.5-fold) was observed for Opto2B mice
449 and Opto2B/GluN2A-KO animals (Fig. 5a,b and Supplementary Table 4), indicating a lack of
450 GluN2A-NMDARs. In fact, the extent of photo-potentiation observed on tonic NMDAR
451 currents was similar to that observed *in vitro* in GluN2B-R187C transduced cultured neurons
452 ($I_{365\ nm}/I_{530\ nm}$ = 3.30 ± 0.39, n = 15 for P8-P12 Opto2B slices, Fig. 5b and Supplementary
453 Table 4, *vs* $I_{365\ nm}/I_{525\ nm}$ = 3.04 ± 0.25, n = 20 for GluN2B-R187C-expressing cultured cortical
454 neurons, Extended Data Fig. 8 and Supplementary Table 1). Therefore, at early postnatal
455 ages, extrasynaptic NMDARs are almost entirely GluN2B diheteromers. Strikingly, for older
456 Opto2B animals (after P12), the photomodulation drastically dropped (to levels close to 1.5-
457 fold), while it was maintained at high levels for Opto2B/GluN2A-KO animals (Fig. 5a,b and
458 Supplementary Table 4). This drop in photomodulation could not be accounted for a
459 progressive decrease in tonic NMDA currents with age (there was instead an increase of
460 APV-dependent tonic current with age; Extended Data Fig. 10c,d). Rather, the
461 developmental drop of photomodulation ratio for Opto2B neurons was mediated by a
462 decrease of the absolute amplitude of UV-induced peak currents (Extended Data Fig. 10e).
463 Altogether, these results show that the proportion of GluN2B diheteromers at extrasynaptic
464 sites strongly decreases with age, and that GluN2B diheteromers are progressively replaced
465 by GluN2A-NMDARs.

466

467 # Discussion

468 As increasing evidence reveal that most neurotransmitter receptors assemble as heteromers
469 with multiple subunit stoichiometries, developing tools to selectively control and monitor
470 individual receptor subtypes becomes a growing challenge[4,6,8,9,69–71]. We have developed an
471 optopharmacological tool (Opto2B) to enhance selectively the activity of NMDARs containing
472 two copies of the GluN2B subunit (GluN2B diheteromers), while receptors containing a single
473 GluN2B copy (GluN2B-containing triheteromers) are unaffected. Opto2B relies on the
474 covalent reaction of a photoswitchable spermine, MASp, to a cysteine-modified GluN2B
475 subunit, GluN2B-R187C. We show that, when bound to GluN2B-R187C, MASp allows fast,
476 reversible and reproducible photo-enhancement of GluN2B diheteromer activity in
477 recombinant systems, cultured neurons and brains slices with minimal off-target effects on
478 basal synaptic transmission. Using this tool, we were able to investigate the evolution of
479 NMDAR subtype composition during postnatal development. We reveal that at hippocampal
480 CA1 pyramidal cells both synaptic and extrasynaptic populations undergo synaptic
481 maturation through a GluN2B-to-GluN2A switch mechanism, but that this maturation occurs
482 at a later time for extrasynaptic populations. At adult stage, our works indicates that GluN2A-
483 containing NMDARs, i.e. GluN2A diheteromers and GluN2A/GluN2B triheteromers, likely
484 form the majority of NMDAR subtypes in hippocampal CA1 neurons at both synaptic and
485 extrasynaptic sites.

486

487 **Opto2B, a GluN2B-selective PAM with subunit stoichiometry resolution**

488 To our knowledge, Opto2B is the first tool allowing the discrimination between NMDAR
489 containing distinct stoichiometries of GluN2A and GluN2B subunits, the two main GluN2
490 subunits in the adult forebrain[16]. Currently available GluN2A-selective NAMs acting at the
491 level of the NTDs (zinc ions) or GluN2A-selective PAMs, have intermediate effects on
492 GluN2A/GluN2B triheteromers. In addition, effects of GluN2A-selective NAMs acting at the
493 LBD level (e.g. TCN-201[72] or MPX-004[73]) are almost as large on GluN2A/GluN2B
494 triheteromers as on GluN2A diheteromers[25,27,74,75]. On the other hand, ifenprodil derivatives,
495 commonly used GluN2B-selective inhibitors, have an intermediate effect on GluN2A/GluN2B
496 triheteromers[25,27]. Polyamines, the only known GluN2B-selective PAMs, have a large
497 potentiating effect on GluN2B diheteromers[28,46], with minimal potentiation of GluN2A/GluN2B
498 triheteromers[27,76]. However, these compounds also produce a non-selective inhibition of all
499 NMDAR subtypes through a pore block mechanism. They furthermore have multiple non-
500 specific effects on various membrane receptors and channels, which might interfere with the
501 GluN2B specific potentiating effect and complicate their use in native systems[29,77,78]. In

502 contrast, the Opto2B tool relies on the covalent binding of a polyamine ligand, MASp, near
503 the GluN2B-specific polyamine potentiating site. After labeling and extensive washout of the
504 free compound, only the bound-MASp remains, hence avoiding off-target pore block of
505 NMDARs, as well as off-target binding to other receptors in native tissues. Accordingly, unlike
506 free spermine, treatment of non-GluN2B NMDARs (GluN2A, 2C and 2D diheteromers) with
507 MASp yielded no light-dependent effect on their activity (Fig. 2). Interestingly, covalent
508 binding of MASp to GluN2B-R187C in the context of a GluN2A/2B triheteromer did not either
509 photosensitize the activity of this receptor subtype. This is reminiscent of the poor effect of
510 free spermine on GluN2A/2B triheteromers (see above) and is consistent with the GluN2A
511 subunit dominating the biophysical and pharmacological properties of GluN2A/2B
512 triheteromers[25,27,75].

513 Despite the exquisite selectivity of Opto2B towards GluN2B diheteromers, MASp can
514 conjugate to the endogenous cysteine GluN2B-C395 in recombinant systems (Xenopus
515 oocytes and HEK cells), leading to an increase in channel Po but no light sensitivity. This
516 increase in basal Po explains the smaller UV potentiation observed when MASp was able to
517 react with both cysteines at positions 187 and 395 (GluN1/GluN2B-R187C receptors; 1.75-
518 fold UV-potentiation in HEK cells) than when C395 reactivity was neutralized, allowing
519 conjugation of MASp only at position R187 (GluN1/GluN2B-R187C-C395S receptors) (3 to
520 3.7-fold UV-potentiation in HEK cells) (Extended Data Fig. 3 and 8a). However, in cultured
521 cortical neurons, whether C395 was neutralized or not had no significant impact on the
522 photomodulation ratio (Extended Data Fig. 8b). Moreover, we obtained large
523 photomodulation ratios in brain slices from Opto2B mice (Fig. 5), close to the ones obtained
524 from cortical brain slices electroporated with the GluN2B-R187C-C395S subunit. This
525 suggests that background conjugation of MASp to the endogenous cysteine GluN2B-C395 is
526 not an issue in native systems. The factors underlying the lack of reactivity of GluN2B-C395
527 in neurons compared to other (non-neuronal) cells remain to be established.

528

529 **Monitoring GluN2B diheteromers with subcellular precision**

530 In addition to its exquisite molecular specificity, the fast and reversible properties of the
531 Opto2B tool allowed us to probe independently, within the same cell, the molecular
532 composition of synaptic and extrasynaptic NMDARs. It is considered that NMDA-EPSCs
533 evoked by single electrical stimulations of presynaptic afferents reflect the activity of the
534 synaptic pool of NMDARs[51]. On the other hand, NMDA tonic currents, recorded in absence of
535 any electrical stimulation, are considered to be mediated primarily by extrasynaptic
536 receptors[49,51,53]. Hence, by measuring in CA1 pyramidal neurons the amount of UV-induced

537 potentiation of NMDA-EPSCs on one side, and NMDA tonic current on the other, we were
538 able to monitor the proportion of GluN2B diheteromers from the CA3-CA1synaptic pool and
539 the extrasynaptic pool, respectively.

540 In many respects, Opto2B outperforms previous methods to investigate the molecular
541 nature of NMDARs. In particular, with its ability to reveal with high sensitivity the presence of
542 extrasynaptic GluN2B diheteromers activated by very low concentrations of ambient
543 glutamate, Opto2B circumvents many limitations of classical pharmacology. Investigation of
544 the molecular nature of extrasynaptic NMDARs has largely relied on classical pharmacology,
545 assessing the extent of tonic NMDAR current inhibition by subunit-specific NMDAR
546 antagonists like zinc or ifenprodil (see, for example, ref. [50]). NMDAR-dependent tonic
547 currents are usually small (30-60 pA) and inhibitors typically take minutes to elicit their effect
548 in brain slices, making the quantification of tonic current inhibitions challenging. In addition,
549 modulation by subunit-specific NMDAR antagonists is usually agonist-dependent, resulting in
550 large variations in the amplitude and direction of modulation depending on agonist
551 concentration. For instance, at low (~100 nM) glutamate concentrations, ifenprodil has a
552 potentiating rather than an inhibitory effect on GluN2B-NMDARs[59]. Similarly, the extent of
553 zinc inhibition strongly depends on the occupancy of the glutamate sites[79,80]. Thus, the
554 effects of conventional pharmacological agents on tonic NMDA currents, which are activated
555 by ambient glutamate concentrations that likely differ from preparation to preparation[56],
556 appear to be unreliable readouts for determining the receptor subunit composition.

557 The Opto2B tool also harnesses the power of light and allows temporal segregation of
558 GluN2B diheteromer potentiation (occurring in a 15 ms time range) linked to the increase in
559 channel Po, from a 10-time slower receptor “depotentiation”, reflecting glutamate dissociation
560 due a decrease in glutamate affinity. The time separation between these two opposite effects
561 yields a clear sharp peak following illumination of the NMDA tonic current. The large
562 amplitude of the current peak (tens of pA) and its independence on glutamate concentration
563 allows reliable estimation of the contribution of GluN2B diheteromers at extrasynaptic sites
564 and its direct comparison with the contribution of this receptor subtype at synaptic sites. On
565 the other hand, the amount of UV-induced potentiation of NMDA tonic currents at steady-
566 state, which strongly depends on glutamate concentration, allows estimation of glutamate
567 concentrations at the vicinity of the receptors (Extended Data Fig. 7). With its unique
568 properties, the Opto2B tool appears well suited to compare NMDAR subunit composition
569 from different cell compartments and to probe the local glutamate microenvironment.

570

571 **Opto2B reveals distinct developmental profiles of synaptic and extrasynaptic NMDARs**

572 Decades of research have established that the GluN2B subunit is enriched at embryonic
573 stages while expression of the GluN2A subunit gradually increases following birth, resulting
574 in a GluN2A/GluN2B ratio that increases with age[7,16,23,50,60,67,81]. However, what is still unclear
575 and highly debated is how the GluN2B subunit partitions between GluN2B diheteromers or in
576 GluN2A/GluN2B triheteromers during brain maturation. Early studies based on subunit co-
577 immunoprecipitation concluded that, at adult stage, the GluN2B subunit is either incorporated
578 preferentially in GluN2B diheteromers[82,83], or, in contrary, in GluN2A/GluN2B triheteromers[84]
579 (see also ref [20]). At adult CA3-CA1 hippocampal synapses, several studies have indicated
580 that the majority of receptors are GluN2A/GluN2B triheteromers (and thus that GluN2B
581 diheteromers are a minority)[20,81,85,86]. Yet, more recently, super-resolution microcopy data on
582 cultured hippocampal neurons revealed a maximum of ~30% of GluN2A and GluN2B subunit
583 colocalization at synaptic sites, suggesting preferential incorporation of GluN2A and GluN2B
584 subunits into diheteromers[87]. In absence of tools with subunit stoichiometry resolution,
585 functional investigations of NMDAR subunit composition is challenging (see above). The
586 Opto2B tool solves this issue in a large part by allowing direct probing of GluN2B
587 diheteromer content.

588 We generated a knock-in mouse expressing the mutated GluN2B-R187C subunit to
589 allow the investigation of the developmental regulation of GluN2B diheteromers at synaptic
590 and extrasynaptic sites, while keeping endogenous levels of GluN2B subunit expression.
591 Using Opto2B mice, we observed an increase of NMDA-EPSC amplitude under UV light at
592 all ages, demonstrating that GluN2B diheteromers are present at CA3-CA1 synapses
593 throughout. However, we also observed a clear decrease of the extent of photomodulation
594 with age reflecting a decreased contribution of synaptic GluN2B diheteromers during
595 development, so that this population becomes a minority at adult stage. Even at early stages,
596 the UV photomodulation remained modest in amplitude (compared to the photomodulation
597 observed on 'pure' GluN2B diheteromers), indicating a scarcity of GluN2B diheteromers.
598 Combining the Opto2B mouse line with the GluN2A-KO mouse line revealed that GluN2A-
599 NMDARs (GluN2A diheteromers and/or GluN2A/GluN2B triheteromers) are indeed already
600 present with GluN2B diheteromers at early postnatal ages (<P12) at the CA3-CA1 synapse.
601 Therefore, following birth, GluN2A-NMDARs readily access synaptic sites (Fig. 6a). For the
602 youngest age tested (P5), the low photomodulation could additionally be linked to the
603 contribution of residual (spermine-insensitive) GluN2D-containing receptors[88], with the
604 GluN2D subunit being highly expressed at embryonic stages before rapidly declining during
605 the first postnatal week in CA1 pyramidal cells[60,88]. Altogether our results demonstrate a
606 gradual disappearance of GluN2B diheteromers at CA3-CA1 synapses during development
607 in favor of GluN2A-containing NMDARs (either GluN2A diheteromers or GluN2A/GluN2B

608 triheteromers, Fig. 6), in line with the previously described GluN2B-to-GluN2A developmental
609 switch. They also add the new information that CA3-CA1 synaptic sites do not favor the
610 clustering of GluN2B diheteromers, but rather of GluN2A-containing receptors, even at early
611 postnatal stages when GluN2B expression still dominates that of GluN2A. This poses key
612 questions that remain to be addressed about the rules governing NMDAR subunit assembly
613 and their specific targeting to distinct neuronal compartments.

614 In contrast to synaptic receptors, we observed that GluN2B diheteromers form the
615 vast majority of extrasynaptic NMDAR subtypes in CA1 pyramidal neurons at young
616 postnatal ages (< P12), which is consistent with the literature[51,58]. At these juvenile ages, our
617 results on Opto2B/GluN2A-KO mice show that GluN2A-NMDARs do not contribute or
618 minimally to NMDA tonic currents (Fig. 6). However, we also observed that the contribution to
619 tonic current of GluN2B diheteromers decreases drastically through development,
620 Opto2B/GluN2A-KO mice revealing a growing contribution of GluN2A-NMDARs at
621 extrasynaptic sites. At adult stage, our results show that GluN2B diheteromers form only a
622 minor population of extrasynaptic NMDARs, while GluN2A-NMDARs predominate (Fig. 6). At
623 first glance, this result challenges the commonly admitted view that GluN2A-NMDARs and
624 GluN2B-NMDARs segregate in synaptic and extrasynaptic compartments, respectively[50,89–91].
625 Several studies, however, do not support such a strict differential repartition, with equivalent
626 GluN2A and GluN2B contents in both compartments[92–95]. This discrepancy likely originates
627 from different methodological approaches, various preparations (neuronal culture or brain
628 slices), brain regions and developmental stages of the studied systems[51]. The limitations of
629 classical pharmacological agents to study extrasynaptic receptors and their complex effects
630 at low agonist concentrations (see above) add to the lack of consensus. Leveraging the
631 unique attributes of Opto2B, we here establish that, similarly to synaptic NMDARs,
632 extrasynaptic NMDARs also undergo a marked GluN2B-to-GluN2A switch in hippocampal
633 CA1 pyramidal cells. The comparison between synaptic and tonic photomodulations also
634 reveals a previously unknown shift in the developmental profile of NMDAR molecular
635 composition between synaptic and extrasynaptic sites (Fig. 4 and 5): GluN2A is incorporated
636 earlier at the synapse but surprisingly constitutes a major part of all NMDARs in the adult
637 mouse at both sites (see model, Fig. 6). These results challenge the prevailing idea of an
638 enrichment of extrasynaptic receptors in GluN2B diheteromers throughout development.
639 Given the robust expression of GluN2B subunit in the adult forebrain[60–62], we propose that a
640 substantial pool of synaptic but also of extrasynaptic NMDARs is constituted by
641 GluN2A/GluN2B triheteromers. Establishing the molecular identity of the various pools of
642 NMDARs, each of which presumably triggers distinct signaling pathways[7,16,23], remain of
643 prime importance to untangle the complex effects of subtype-specific NMDAR signaling on

644 brain circuits and behavior. It also provides valuable information for the design and biological
645 understanding of precision pharmaceutics targeting NMDARs[2,17].

646 In conclusion, we have engineered, validated and implemented a new tool, Opto2B,
647 that enables fast and selective interrogation of native GluN2B diheteromers in isolation form
648 other co-expressed NMDARs. Using Opto2B, we established the developmental sequence
649 that shapes the distribution of GluN2A and GluN2B subunits at synaptic and extrasynaptic
650 sites in CA1 pyramidal neurons, while clarifying a long-standing contentious issue, that of the
651 relative abundance of GluN2A- and GluN2B-containing receptors between both locations.
652 We foresee broad applications of Opto2B and other optopharmacological tools targeting
653 NMDARs to study their molecular and functional adaptation to contextual experience and
654 disease states.

655

656 # Methods

657 ## Chemicals

658 Salts, buffers, glucose, D-serine, DTPA (diethylenetriamine-pentaacetic acid), glucose, L-
659 glutamate, glycine, spermine, Mg-ATP and Na-GTP were purchased from Sigma-Aldrich (St.
660 Louis, MO, USA). D-APV (D-(-)-2-Amino-5-phosphonopentanoic acid), NMDA (N-methyl-D-
661 aspartate), NBQX (3-Dioxo-6-nitro-1,2,3,4-tetrahydrobenzo[*f*]quinoxaline-7-sulfonamide),
662 TBOA (DL-*threo*-β-Benzyloxyaspartic acid), strychnine, picrotoxin were purchased from
663 HelloBio (County Meath, ROI). MK801 was purchased from Ascent Scientific (now Abcam,
664 Cambridge, UK). Gentamycin was purchased from GIBCO (Invitrogen, Rockville, MD, USA).
665 Ro 25-6981 is a gift from F. Hoffmann-LaRoche. MPX-004 was purchased from Alomone
666 Labs.

667 Stock solutions of L-glutamate (100 mM), glycine (100 mM), DTPA (10 mM), D-serine
668 (500 mM), NMDA (100 mM), MK801 (50 µM), D-APV (50 or 100 mM), NBQX (10 mM) and
669 strychnine (10 mM) were prepared in bi-distilled water. Picrotoxin (100 mM), MPX-004
670 (30 mM) and Ro 25-6981 (10 mM) stock solutions were prepared in DMSO. All stock
671 solutions were stored at -20 °C.

672

673 ## MASp chemical synthesis and characterization

674 MASp (1-[2-(4-{(E)-[4-(2-{[3-({4-[(3-aminopropyl)amino]butyl}amino)propyl]amino}ethoxy)
675 phenyl] diazenyl}phenoxy)ethyl]-1H-pyrrole-2,5-dione tetrakis(trifluoroacetate)) was obtained
676 as a trifluoroacetate salt from custom synthesis by Spectrum Info Ltd (https://www.spec-
677 info.com/, Kiev, Ukraine; currently available at
678 https://shop.lifechemicals.com/compound/1/F9995-4157). NMR and mass-spectroscopy
679 characterizations are described in Supplementary Note 1. MASp stock solutions were
680 prepared in anhydrous DMSO at concentrations of 16.5 mM (for labeling of Xenopus oocytes
681 and brain slices) or 0.66 mM (for labeling of HEK cells and cultured neurons) and stored at -
682 20 °C.

683

684 ## MASp photochemical characterization

685 To avoid hydrolysis of the maleimide moiety during compound characterization, MASp was
686 reacted in the dark with 2 equivalents of L-cysteine (Sigma-Aldrich) during at least 30 min in
687 oocyte recording Ringer solution at pH 7.3 (see below). This reaction is predicted to produce
688 four different cysteine-conjugated MASp ($MASp^{Cys}$) diastereoisomers (Supplementary Fig. 1).

689 Spectroscopic analyses and HPLC analyses were made on the crude product mixture. All
690 experiments were performed at room temperature.

691 UV-visible absorption spectra were acquired in 1cm long quartz cuvettes on a
692 NanoPhotometer® NP80 spectrometer (Implen, Germany). MASp was diluted at 33 µM in
693 Ringer (pH 7.3) from the 16.5 mM DMSO stock (0.2% DMSO final concentration) solution
694 together with 100 µM L-cysteine to yield $MASp^{Cys}$. Blank solution was Ringer at pH 7.3
695 containing 0.2 % DMSO and 100 µM L-cysteine. Photostationary states (PSS) of $MASp^{Cys}$ *cis*
696 and *trans* isomers were obtained by continuous illumination of the quartz cuvette containing
697 the $MASp^{Cys}$ solution with a multi-wavelength LED (pE-2 and pe-4000, CoolLED, UK) until no
698 further change in the absorption spectra was observed. For all irradiation wavelengths
699 tested, 5 min illumination was sufficient to reach steady state. Photostability of the *cis* state
700 (365 nm PSS) was measured by irradiating the $MASp^{Cys}$ solution with 365 nm light during 10
701 min, then letting it relax in the dark, inside the spectrophotometer. Spectra were acquired at
702 regular intervals, up to 8 h after irradiation.

703 Analytical HPLC was performed on an Agilent 1200 series equipped with a quaternary
704 pump using a Proto 200 C18 column from Higgins Analytical Inc (particles size 3 µm,
705 100×4.6 mm column). The compounds (66 µM of $MASp^{Cys}$ products in Ringer solution) were
706 eluted with a flow of 1 ml/min using a gradient of acetonitrile (0 to 100% over 10 minutes) in
707 water, both solvents containing 0.1% TFA. The detection was performed at 220 nm, 280 nm
708 and 440 nm ($MASp^{Cys}$ isosbestic point, see Figure S1A). $MASp^{Cys}$ *cis*/*trans* PSS in the dark
709 and after illumination with 365 and 525 nm light were determined by HPLC using the relative
710 integrated areas of the *cis* and *trans* peaks at 440 nm. HPLC of a baseline solution
711 containing 0.4 % DMSO and 200 µM L-Cysteine was measured and its chromatogram
712 subtracted to the one of $MASp^{Cys}$. Due to the presence of two diastereoisomers per
713 azobenzene configuration after reaction with cysteine, *trans* and *cis* $MASp^{Cys}$ were each
714 represented by two peaks (see Figure S1C).

715

716 **Molecular biology**

717 For expression in HEK cells and Xenopus oocytes, rat GluN2A and mouse GluN2B subunits
718 (ε2) and eGFP were expressed using pcDNA3-based expression plasmids, and rat GluN1-1a
719 (named GluN1 herein) using pRCCMV plasmid. For selective expression of tri-heteromeric
720 NMDARs, DNAs coding for a modified GluN1 subunit (GluN1-6A) and GluN2A and GluN2B
721 subunits containing the $GABA_B$ retention signals (GluN2A-r1, GluN2B-r1 and GluN2B-r2)
722 were from ref. [27]. Point mutations were performed by Quikchange mutagenesis and DNA
723 sequences verified by Sanger sequencing.

724 For *ex utero* and *in utero* electroporation, mouse GluN2B-R187C-C395S, GluN2B-
725 R187C-C395S-IRES-GFP, GluN2B-R187C-IRES-GFP, Cre, GFP and Td-tomato constructs
726 were expressed using pCAG-based plasmids. pCAG_GFP and pCAG_Td-tomato were from
727 ref. [47]. pCAG_GluN2B-R187C-C395S was obtained by subcloning from the pCAG_GFP and
728 p3αpA_GluN2B-R187C-C395S plasmids using KpnI (ThermoFisher Scientific) and NotI (New
729 England Biolabs) restriction enzymes. pCAG_GluN2B-R187C-C395S-IRES-GFP and
730 pCAG_GluN2B-R187C-IRES-GFP were obtained by Quikchange mutagenesis of the
731 pCAG_GluN2B-IRES-GFP plasmid (a gift from Katherine Roche, ref. [23]).

732

733 **Oocyte preparation and injection**

734 Oocytes from Xenopus *lævis* were used for heterologous expression of recombinant NMDA
735 receptors for two-electrode voltage-clamp (TEVC) experiments. Female Xenopus laevis were
736 housed and ovary bags harvested according to European Union guidelines (husbandry
737 authorizations #C75-05-31 and #D75-05-31; project authorizations #05137.02 and Apafis
738 #28867-2020121814485893). Fragments of ovary bags were also purchased from the
739 "Centre de Ressources Biologiques Xenopes" (now TEFOR, Paris Saclay, France) and from
740 the European Xenopus Resource Center (EXRC, Portsmouth, UK). Xenopus *laevis* oocytes
741 were harvested and prepared as previously described in ref.[96]. Briefly, membranes of ovary
742 bags were teared with forceps to expose the oocytes to the medium. Ovary bag fragments
743 were then subjected to digestion with Collagenase type II (Gibco, 1-1.5 mg/mL) diluted in a
744 calcium-free, OR2 medium (in mM: 85 NaCl, 5 HEPES, 1 $MgCl_2$, pH adjusted to 7.6 with
745 KOH) under mild shaking (~110 rpm) until the oocytes were fully defolliculated (usually after
746 ~1 h). Oocytes were then washed 5 times in OR2 then 3 times with a Barth solution (in mM:
747 88 NaCl, 1 KCl, 0.33 $Ca(NO_3)_2$, 0.41 $CaCl_2$, 0.82 $MgSO_4$, 2.4 $NaHCO_3$ and 7.5 HEPES, pH
748 adjusted to 7.3 with NaOH). Defolliculated oocytes were stored at 12°C in a Barth solution
749 supplemented with gentamycin (50 µg/µL).

750 Expression of recombinant di-heteromeric NMDARs was obtained by oocyte nuclear
751 co-injection of 37 nL of a mixture of cDNAs (at 10-30 ng/µL) coding for GluN1-1a and various
752 GluN2 subunits (ratio 1:1). Expression of tri-heteromeric NMDARs using modified subunits
753 containing the $GABA_B$ ER retention signals was obtained by co-injecting a mixture of cDNAs
754 coding for GluN1-6A, GluN2-r1 and GluN2-r2 subunits at 45 ng/µL (ratio 2:1:1)[27]. Co-injection
755 of a mixture of GluN1-6A/GluN2-r1 or GluN1-6A/GluN2-r2 (45 ng/µL, 1:1 ratio), which is not
756 supposed to yield membrane expression of NMDARs, was systematically performed to
757 monitor leakage of the retention motifs[27]. After injection, the oocytes were transferred to 96-
758 well plates filled with Barth supplemented with gentamicin (50 µg/µL) and 50 µM APV, a

759 selective NMDAR antagonist. Plates were then stored at 18 °C for 24h for expression of
760 GluN1/GluN2A constructs, and 48h to 96h for expression of GluN1/GluN2B, GluN1/GluN2C,
761 GluN1/GluN2D and tri-heteromeric constructs.

762

763 **Oocyte labeling, TEVC recordings and NMDAR photomodulation**

764 *Oocyte labeling*

765 Oocytes (~5 oocytes per 1 mL labeling solution) were labeled in a Barth solution containing
766 0.66 µM MASp (diluted from a 16.5 mM stock, 0.004% DMSO in final dilution) during 15 min
767 on ice (0°C), in the dark, under mild shaking (90 rpm). Oocytes were then thoroughly washed
768 in 4 mL of Barth solution during 10 min in the dark, on ice, under mild shaking (90 rpm),
769 during three consecutive times (30 min total wash time). Oocytes were transferred to a new
770 well containing 4 mL Barth between each washing step. Increasing the labeling step to
771 30 min instead of 15 min did not increase the amplitude of photomodulation. On the other
772 hand, we observed strong non-covalent association of MASp with NMDARs and/or the
773 oocyte membrane, so that increase of MASp concentration in the labeling solution (to
774 6.6 µM) or decrease of the wash time resulted in incomplete washout of the non-covalently
775 bound compound. This was evidenced by a slow inhibition of WT GluN1/GluN2B or
776 GluN1/GluN2A receptor currents by UV light, which was slowly reversed by green light. This
777 effect slowly washed away as the cell was submitted to several illumination cycles. We
778 attributed this slow and non-specific effect on NMDAR currents to a high affinity, photo-
779 dependent pore block. It has indeed been shown that aromatic polyamines induce high
780 affinity inhibition of NMDARs through a pore block mechanism[29,97,98]. Reducing the labeling
781 time, MASp concentration and increasing wash time allowed us to eliminate this non covalent
782 MASp effect, with no effect of light on WT GluN1/GluN2B NMDARs with our final labeling
783 conditions (Fig. 1e).

784 *TEVC recordings*

785 1–4 days following DNA injection, TEVC recordings were performed using an Oocyte Clamp
786 amplifier OC-725 (Warner Instruments) computer-controlled via a 1440A Digidata (Molecular
787 Devices). Currents were sampled at 100 Hz and low-pass filtered at 20 Hz using an 8-pole
788 Bessel filter (900 Series, Frequency Devices Inc). Data were collected with Clampfit 10.3.
789 During the recording, the cells were continuously perfused with external recording Ringer
790 solution at either pH 7.3 (in mM: 100 NaCl, 0.3 $BaCl_2$, 5 HEPES and 2.5 KOH, pH adjusted to
791 7.3 by addition of HCl) or 6.5 (in mM: 60 NaCl, 0.3 $BaCl_2$, 40 HEPES, 2.5 KOH, pH adjusted
792 to 10.3 with NaOH, then back to 6.5 with HCl, see ref [28]). Unless otherwise noted, NMDA

793 currents were induced by simultaneous application of L-glutamate and glycine (agonist
794 solution) at saturating concentration (100 µM each), and DTPA (10 µM) to prevent receptor
795 inhibition by ambient zinc (~20 nM, ref. [80]). Control, agonist free solution contained 10 µM
796 DTPA. All recordings were performed at a holding potential of -60 mV and at room
797 temperature.

798 *Photomodulation*

799 Photomodulation of NMDA currents on Xenopus oocytes was performed by irradiating the
800 oocyte from the top (irradiation of the animal pole) during TEVC recording with a PE-2 light
801 source (CoolLED) coupled to a liquid light guide, using wavelengths of either 365 nm
802 (irradiance ~ 8 mW/mm^2) or 490 nm (irradiance ~ 18 mW/mm^2).

803 *Pharmacological characterization of NMDAR mutants*

804 Pharmacological characterization was performed on unlabeled oocytes, or on MASp-labeled
805 oocytes in the dark or under constant illumination with 365 or 490 nm light. Glutamate and
806 glycine dose-response curves were recorded at pH 7.3. Glutamate dose-response curves
807 were performed in presence of 100 µM glycine and varying concentrations of glutamate.
808 Glycine dose-response curves were performed in presence of 100 µM glycine and varying
809 concentrations of glutamate. For each cell, agonist dose-response curves were fitted with the
810 Hill equation: $I = I_{max} / (1 + (EC_{50}/[A])^{nH})$, where I_{max} is the maximum current calculated from
811 the fit, EC_{50} the agonist concentration necessary to induce 50 % of I_{max}, n_H is the Hill
812 coefficient, and [A] the agonist concentration. I_{max}, n_H and EC_{50} were fitted as free
813 parameters. Proton dose-response curves were performed and analyzed as previously
814 described[99]. Spermine sensitivity was assessed by measuring currents in absence and in
815 presence of 200 µM spermine at pH 6.5, as previously described[28]. Open probability (Po) of
816 the different NMDAR mutants was assessed by measuring the rate of inhibition by 100 nM
817 MK801, an open channel blocker whose inhibition kinetics correlate with channel Po[34–38].
818 Recordings were performed at acidic pH (6.5) to maximize the differences of Po between the
819 MASp-potentiated and non-potentiated receptors. MK-801 time constants of inhibition (τ_{on})
820 were obtained by fitting inhibition currents with a single-exponential function. On-rate (k_{on})
821 constants were then calculated assuming a pseudo first-order reaction scheme: $k_{on} = 1 /$
822 $([MK\text{-}801]*\tau_{on})$. In Extended Data Fig. S2g, all k_{on} were normalized to the average k_{on} of
823 untreated, wt GluN1/GluN2B receptors measured in the same conditions on the same day.

824

825 **Mice**

826 Mice were housed in the IBENS rodent facility duly accredited by the French Ministry of
827 Agriculture. All experiments were performed in compliance with French and European
828 regulations on care and protection of laboratory animals (EU Directive 2010/63, French Law
829 2013-118, February 6th, 2013), and were approved by local ethics committees and by the
830 French Ministry of Research and Innovation (authorization numbers #05137.02, APAFIS
831 #28867-2020121814485893 and APAFIS #29476-2021020311595454). Animals were
832 maintained on a 12-hour light/dark cycles with food and water provided *ad libitum*.

833 For *ex vivo* experiments performed in the cortex, *in utero* electroporation was performed on
834 time-pregnant Swiss mice and both male and female pups we used for recordings. For *ex*
835 *vivo* recordings in the hippocampus, both male and female mice were used as well with their
836 corresponding littermates from the following lines: WT C57Bl/6N, GluN2B-R187C KI (Opto2B
837 mouse, generated in this study, see below), GluN2A KO[66], and Opto2B/GluN2A-KO
838 generated by crossing the Opto2B and GluN2A KO lines. Opto2B mice are on a C57Bl/6N
839 background, GluN2A KO mice on a C57Bl/6J background, and Opto2B/GluN2A KO mice on
840 a mixed C57Bl/6N and C57Bl/6J background. For neuronal culture experiments, WT
841 C57Bl/6J mice or floxed-Grin2B transgenic mice (B6.Cg-Grin2btm1Mony/Crl, ref. [100]) were
842 used. All the mice used in our experiments were homozygous for their corresponding
843 gene(s).

844

845 *Generation of the Opto2B mouse and determination of genotype*

846 The Opto2B mouse, containing the GluN2B-R187C mutation, was generated by the *Institut*
847 *clinique de la souris*, Phenomin (Illkirch, France) using the CRISPR/Cas9 strategy. At the
848 position equivalent to R187 on GluN2B, codon CGC was replaced by TGC, leading to
849 substitution of an arginine to a cysteine. The C>T substitution also created a BglII enzyme
850 restriction site, which was used to discriminate WT and mutant animals during genotyping
851 (AGATC***T***, the T in bold italic being the substituted base).

852 Genotyping consisted of several steps. DNA was first dissociated in 25 mM NaOH during 1
853 hour at 93°C and the reaction was stopped with 40 mM TrisHCl. DNA was then amplified by
854 PCR (DreamTaq DNA Polymerase EP0705 Thermofischer - $MgCl_2$ 1 mM R0971
855 Thermofischer - 0.2 mM dNTP R0193 Thermofischer; 34 cycles: 30 s at 94°C, 30 s at 62°C,
856 60 s at 72°C, 1 min at 72°C) using primers TCTGTCATGCTCAACATCATGGAAG and
857 GATGGCAATCCCATCTCTCACTCTG. DNA products were then digested overnight using
858 0.1 U/µL of restriction enzyme BglII (New England Biolabs). Discrimination between
859 genotypes was performed on a gel electrophoresis according to the presence or absence of

860 WT (undigested bands, expected molecular weight: 435 bp) and digested mutant GluN2B
861 characteristic bands (expected molecular weights: 341 and 94 bp).

862

863 **Dissociated cell culture and transfection/electroporation**

864 *HEK cells*

865 HEK-293 cells (obtained from ECACC, Cat #96121229) were cultured in DMEM + glutamax
866 medium supplemented with 10% fetal bovine calf serum and 1% Penicillin/streptomycin
867 (5000 U/ml), under standard cell culture conditions (5% CO_2, 37 °C). Transfections were
868 performed using polyethylenimine (PEI, linear 25 kD; Polysciences, Inc., Eppelheim,
869 Germany; stock at 1mg/mL) with a cDNA/PEI ratio of 1:3 (v/v). Cells were co-transfected with
870 a DNA-mixture containing plasmids encoding wild-type GluN1, GluN2A or GluN2B
871 constructs, and eGFP. The total amount of DNA was 1.0 µg per 500 µL of transfected
872 medium for a 12 mm² diameter coverslip The DNA mass ratio for GluN1:GluN2B:eGFP was
873 1:2:1 and 1:1:1 for GluN1:GluN2A:eGFP. 150 µM of D-APV was added to the culture medium
874 after transfection. Currents from HEK cells expressing GluN1/GluN2A and GluN1/GluN2B
875 constructs were recorded 24h and 48-72h post transfection, respectively.

876

877 *Cortical neurons*

878 Dissociated cultures of cortical neurons were prepared from mouse embryos at E15. After
879 brain extraction, expression of GluN2B-R187C-C395S mutated subunit in cortical was
880 performed by *ex utero* electroporation. Endotoxin-free cDNAs coding for GluN2B-R187C-
881 C395S (pCAG_GluN2B-R187C-C395S plasmid, 0.5 µg/µL) and for a GFP fluorescent marker
882 (pCAG_GFP plasmid, 0.5 µg/µL) were injected unilaterally into the lateral ventricle of the
883 mouse embryos using a glass pipette. For experiments using the Cre-Lox strategy, GluN2B-
884 R187C-C395S (pCAG_GluN2B-R187C_IRES_GFP, 1 µg/µL) or GluN2B-R187C
885 (pCAG_GluN2B-R187C_IRES_GFP, 1 µg/µL) subunits were expressed as well as a Cre-
886 recombinase (pCAG_Cre, 1 µg/µL) on floxed-Grin2B mice[100] following the same protocol. As
887 the GFP fluorescence from IRES constructs was barely visible, a Td-Tomato fluorescent
888 marker (pCAG_Td-Tomato, 1 µg/µL) was systematically co-electroporated. The volume of
889 injected DNA was adjusted depending on the experiments. Electroporation was performed
890 using a square wave electroporator (ECM 830, BTX) and tweezer-type platinum disc
891 electrodes (5mm diameter, Sonidel). The electroporation settings were: 5 100ms-long pulses
892 at 18 V separated by 100 ms.

After removing meninges, electroporated cortices were placed in ice-cold HBSS solution supplemented with 20 mM HEPES. Cell dissociation was performed individually for cortices of each embryo. Cortices were incubated in 2.5% trypsin at 37 °C for 10 min, rinsed three times with 37 °C HBSS solution, and further dissociated by trituration with syringes of decreasing diameter (21 then 24 gauge). Cells were resuspended in attachment medium (MEM supplemented with 2 mM glutamine, 1% penicillin/streptomycin (5000 U/ml), 1 mM sodium pyruvate and 10 % horse serum) then plated on poly-D-lysine coated coverslips in 24-well culture dishes at a density of 1-2*10^5 cells per well. Cells were cultured under standard cell culture conditions (37°C, 5% CO_2). Attachment medium was changed to Neurobasal medium (MEM supplemented with 2 mM L-glutamine, 1% B27 supplement and 1% Penicillin/Streptomycin) 2 hours after plating. Cells were fed by changing ½ medium to fresh Neurobasal medium every 4 days. Cultures were used for experiments after 6 to 9 days *in vitro* (DIV6 to DIV9).

Labeling and patch-clamp electrophysiology on dissociated cells

Before patch-clamp recording, HEK cells and cultured cortical neurons were labeled with MASp. Labeling was performed by incubating the coverslips in 500 µM of extracellular recording solution (in mM: 140 NaCl, 2.8 KCl, 1 $CaCl_2$, 10 HEPES, 20 sucrose and 0.01 DTPA; 290–300 mOsm; pH adjusted to 7.3 using NaOH) containing 0.66 µM MASp (0.1% final DMSO concentration) at 37°C in the cell culture incubator. Coverslips were then transferred into a petri dish containing ~4 mL extracellular recording solution, then to the patch-clamp recording chamber.

Whole-cell patch-clamp recordings were performed on an Olympus IX73 inverted microscope. Positively transfected cells were visualized by GFP fluorescence. Patch pipettes had a resistance of 3–6 MΩ and were filled with a solution containing (in mM): 115 CsF, 10 CsCl, 10 HEPES and 10 BAPTA (280–290 mOsm), pH adjusted to 7.2 using CsOH. Currents were sampled at 10 kHz and low-pass filtered at 2 kHz using an Axopatch 200B amplifier, a 1550B digidata and Clampex 10.6 (Molecular Devices). Recordings were performed at a holding potential of −60 mV and at room temperature. Agonists (100 µM glutamate and glycine for HEK cells; 300 µM NMDA and 50 µM D-serine for cortical neurons) were applied using a multi-barrel solution exchanger (RSC 200, BioLogic). In Figure S4A, NMDAR currents from cultured cortical neurons were elicited by varying concentrations of glutamate and glycine and isolated by adding 10 µM NBQX, 100 µM picrotoxin, 10 µM strychnine, and 20 µM glycine to the extracellular recording solution, in order to mimic the recording conditions of neurons in brain slices (see below).

928 Computer-controlled light pulses during electrophysiological recordings were provided
929 from high power LEDs (Prizmatix). The three following LEDs were used: Mic-LED-365
930 (365 ± 4 nm, 200 mW), UHP-Mic-LED-460 (460 ± 5 nm, 2 W) and UHP-Mic-LED-520
931 (520 ± 5 nm, 900 mW). The LED port was directly coupled to the fluorescence port of the
932 microscope. The output beam of the LED entry was directed towards the sample thanks to a
933 mirror (Chroma) and applied to the center of the recording dish through a 10X objective
934 (Olympus, 0.30 N.A.). In Extended Data Fig. 3g, light power was measured at the center of
935 the recording chamber plane with an optical power meter (1916-C, Newport) equipped with a
936 calibrated UV/D detector.

937

938 ***In utero* electroporation**

939 *In utero* electroporation was performed as previously described[47]. Briefly, pregnant Swiss
940 females at E14.5-15.5 (Janvier labs) were subcutaneously injected with 0.1 mg/kg of
941 buprenorphine for analgesia and anesthetized with isoflurane (3.5% for induction and 2%
942 during the surgery). The uterine horns were exposed after laparotomy. Endotoxin-free DNA
943 diluted in 1× PBS with 0.1% Fast Green dye for visualization was injected unilaterally into the
944 lateral ventricle of the mouse embryos using a glass pipette. The volume of injected DNA
945 was adjusted depending on the experiments. Electroporation was performed using a square
946 wave electroporator (ECM 830, BTX) and tweezer-type platinum disc electrodes (5 mm
947 diameter, Sonidel). The electroporation settings were: 5 pulses of 50 V for 50 ms with 500 ms
948 interval. DNAs were used at the following concentration: pCAG_Td-tomato, 1 µg/µL;
949 pCAG_GluN2B-R187C-C395S, 2 µg/µL.

950

951 ***Ex vivo* patch clamp electrophysiology**

952 *Slice preparation and labeling*

953 Acute coronal slices (320 µm) were prepared at the indicated age by decapitation of the
954 isoflurane-anesthesized animals. After brain extraction, slices were prepared using a
955 vibratome (Leica VT1200S). Slicing was performed in a cold (~ 4°C) and oxygenated (95%
956 O_2, 5% CO_2) slicing solution containing (in mM): 92 choline chloride, 2.5 KCl, 1.2 NaH_2PO_4,
957 30 $NaHCO_3$, 20 HEPES, 25 glucose, 5 ascorbic acid, 3 sodium pyruvate, 10 Magnesium
958 sulfate, 0.5 calcium chloride, pH adjusted to 7.3 by Tris base. Slices were transferred to an
959 ACSF solution (in mM: 125 NaCl, 2.5 KCl, 1.25 NaH_2PO_4, 26 $NaHCO_3$, 20 D-glucose, 2
960 $CaCl_2$, 1 $MgCl_2$) at 32°C under constant oxygenation and left to recover for 1-1.5 hours.
961 Labeling was performed by incubating the slices in oxygenated ACSF containing 6.6 µM

962 MASp (from 16.5 mM stock, 0.04% DMSO in final dilution) during 30 min at 32°C. Slices
963 were then kept in ACSF before recording.
964
965 *Electrophysiology*

966 Slice electrophysiology was performed on a Scientifica SliceScope upright microscope
967 coupled to an OrcaFlash 4.0 camera for cell and fluorescence visualization. Electroporated
968 cells were identified by their Td-tomato fluorescence. Whole-cell patch-clamp recordings
969 were performed at ~28-30°C in either layer 2/3 cortical pyramidal neurons of the
970 somatosensory cortex or CA1 pyramidal neurons of the hippocampus. Currents and
971 potentials were recorded using a Multiclamp 700B amplifier coupled to a 1550B Digidata and
972 Clampex 10.6 (Molecular Devices). Currents were sampled at 10 kHz. Patch pipettes
973 (Hilgenberg) had a resistance of 3 to 6 MΩ.

974 For voltage-clamp recordings, cells were patched using the following intracellular
975 solution (in mM): 125 CsMeSO4, 10 BAPTA, 5 TEA, 10 HEPES, 4 Mg-ATP, 0.2 Na_3-GTP
976 (280-290 mOsm, pH adjusted to 7.3 using CsOH). Series resistance (typically < 20 MOhm
977 before compensation) was compensated (around 40-60%) and monitored during the whole
978 experiment. Extracellular synaptic stimulation was achieved by applying voltage pulses (3.5
979 ms, 5–50 V; Digitimer Ltd, UK) via a second patch pipette filled with HBS (in mM: 150 NaCl,
980 2.5 KCl, 1.25 NaH_2PO_4, 10 HEPES, 2 $CaCl_2$, 1 $MgCl_2$; pH adjusted to 7.4 with NaOH) and
981 placed near the apical dendrite of the patched neuron (for cortical neurons[47]), or by
982 stimulating the afferent Schaeffer collaterals in the *stratum radiatum* for CA1 hippocampal
983 neurons. AMPA currents were recorded at -70 mV in ACSF. NMDA currents (NMDA EPSCs
984 and tonic currents) were recorded at +40 mV and isolated by adding 10 µM NBQX, 100 µM
985 picrotoxin, 10 µM strychnine and 20 µM glycine to ACSF (as in ref. [101]). NMDA/AMPA ratios
986 were recorded in regular ACSF and calculated as the ratio of EPSC amplitude at +40 mV
987 holding potential measured 50 ms after peak (NMDA component) over EPSC at peak at -
988 70 mV holding potential (AMPA component).

989 For current clamp experiments patch pipettes were filled with the following
990 intracellular solution (in mM): 130 K-gluconate, 5 KCl, 10 HEPES, 0.6 EGTA, 2 $MgCl_2$, 0.2
991 $CaCl_2$, 2 Mg-ATP, 0.3 Na_3-GTP (290-300 mOsm, pH adjusted to 7.3 using KOH). Cell
992 hyperpolarization/depolarization and action potentials were induced by 500 ms current
993 injections ranging from -300 to +800 pA.

994 *Photomodulation and analysis of light-dependent effects*

995 Computer-controlled light pulses during electrophysiological recordings were provided from
996 ThorLabs LEDs. The two following LEDs were used: M365L2 (365 nm) and M530L3
997 (530 nm). The LED port was directly coupled to the fluorescence port of the microscope. The
998 output beam of the LED entry was directed towards the sample thanks to a mirror (Chroma)
999 and applied to the center of the recording chamber through a 40X objective (Olympus, 0.1
1000 N.A.). We observed that UV light at high power abolished synaptic transmission. UV light
1001 intensity was thus chosen so that in induces minimal decrease of synaptic transmission while
1002 still allowing photomodulation. Final powers measured in the recording chamber for UV and
1003 green light illuminations were ~2 mW for 365 nm light and ~0.3 mW for 530 nm.

1004 Effect of light on NMDA EPSCs was monitored by illuminating the region around the
1005 patched neuron 1s before stimulation until 200 ms after stimulation (1.2 s total illumination).
1006 Photomodulation ratios were measured by performing cycles of five stimulations at 0.1 Hz
1007 with green (530 nm) light, followed by five stimulations at 0.1 Hz with UV (365 nm) light,
1008 followed by three other green-UV-green cycles (Extended Data Fig. 5a). Due to the slow
1009 reversal of UV-induced potentiation by green light, steady-state current under green light was
1010 obtained only after the third green light illumination bout (see Extended Data Fig. 5a). As a
1011 consequence, the average of only the last three EPSCs of the five-stimulation cycles (either
1012 with UV or green light) were considered to calculate the photomodulation ratios (Extended
1013 Data Fig. 5a, grey bars). For cortical neurons, photomodulation ratios were calculated as the
1014 ratios of the mean EPSC amplitude under UV light (3 EPSCs x 2 UV cycles = 6 EPSCs) over
1015 the mean EPSC amplitude under green light (3 EPSCs x 3 green cycles = 9 EPSCs). The
1016 same protocol and data analysis were applied to investigate the photodependence of AMPA
1017 EPSCs after MASp treatment of the slice (Extended Data Fig. 5d). For hippocampal neurons,
1018 the absolute NMDA-EPSC responses decreased after the first green-UV-green cycle for
1019 some cells. Hence, to decrease cell-to-cell variability, only the first green-UV-green cycle was
1020 taken into account to calculate the photomodulation ratio (meaning 3 EPSCs x 1 UV cycle =
1021 3 EPSCs in UV light and 3 EPSCs x 2 green cycles = 6 EPSCs in green light).

1022 NMDA-EPSC decay time constants (τ_w NMDA-EPSC) were calculated by fitting the
1023 decay phase of the averaged EPSCs under green light with a double exponential using the
1024 following formula: $I = I_0 + A_{fast}.\exp\left(\frac{-(t-t_0)}{\tau_{fast}}\right) + A_{slow}.\exp(\frac{-(t-t_0)}{\tau_{slow}})$, where τ_{fast} and τ_{slow}
1025 represent the fast and slow time constants of EPSC decay, respectively, and A_{slow} and A_{fast}
1026 their relative weights. τ_w NMDA-EPSC represents the weighted time constant calculated as
1027 follows: $\frac{A_{fast}}{A_{fast}+A_{slow}}.\tau_{fast} + \frac{A_{slow}}{A_{fast}+A_{slow}}.\tau_{slow}$.

1028 The protocol of photomodulation of tonic currents consisted of 5-10 cycles of 2 s of
1029 365 nm illumination and 4 s of 530 nm illumination, repeated every 30 s (see Fig. 3d and
1030 Extended Data Fig. 6a,c). Cells were maintained in the dark between illumination steps.
1031 Except for Extended Data Fig. S6c, calculations were performed on the average current
1032 trace from the 5 or 10 illumination cycles. APV was systematically applied in the dark after
1033 the 5 or 10 cycles of illumination to allow calculation of photomodulation ratios, and the
1034 illumination protocol was repeated in presence of APV to check for proper inhibition of all
1035 NMDARs, including the photodependent receptors. Since APV was applied in the dark and
1036 after green light illumination, the APV-sensitive current (I_{APV}) represents the basal NMDA
1037 tonic current in the dark or under green light ($I_{APV} = I_{530\ nm}$). Under UV light, NMDA tonic
1038 current is calculated as $\Delta_{UV,\ peak} + I_{APV}$ at the time of peak, with $\Delta_{UV,\ peak}$ representing the UV-
1039 induced increase in tonic current at its peak (~ 35 ms after the onset of UV light, mean
1040 around the peak over a windows of 0.30 ms to avoid bias from nonspecific noise) (see
1041 Extended Data Fig. 6a). The photomodulation ratio was calculated as $(\Delta_{UV,\ peak} + I_{APV})/I_{APV}$
1042 (Fig. 3d). Rising and decaying phases of the UV-induced current peak were fitted with single
1043 exponentials.

1044

1045 **Subtype-specific pharmacology on NMDA-EPSCs**

1046 For Ro 25-6981 or MPX-004 experiments, slices from Opto2B animals were labeled with
1047 MASp but not the ones from WT animals. NMDA-EPSCs were isolated by adding to ACSF
1048 10 µM NBQX, 100 µM picrotoxin, 10 µM strychnine but, contrary to photomodulation
1049 experiments, no glycine was added to maximize the effect of MPX-004[75]. A baseline of
1050 NMDA-EPSCs was recorded for at least 5 min before adding the pharmacological agent.
1051 Ro 25-6981 was applied at 1 µM and MPX-004 at 30 µM. NMDA-EPSCs were recorded for
1052 at least 5 min after the effect of the inhibitors has reached steady state (total duration of
1053 ~30 min). Cells were maintained in the dark. Only cells with stable EPSCs before application
1054 of the inhibitor were analyzed. For each drug, percentage of inhibition effect was calculated
1055 as the ratio between the average of EPSC amplitudes over 3 minutes before drug application
1056 and the average of EPSC amplitudes over 3 minutes once stability is reached after drug
1057 action.

1058

1059 **Data analysis and Statistical analysis**

1060 Electrophysiological data were analyzed using Clampfit 10.3 (Molecular Devices), Prism
1061 (GraphPad software), Igor (Wavemetrics) and a built-in Python script. Graphs were

1062 generated and statistical analyses were performed using Sigmaplot 11, GraphPad Prism 9
1063 and 10, or Python (using Matplotlib[102] – version 3.7.4 -, Seaborn[103] – version 0.13.1 -).
1064 Statistical tests are displayed in the Figure legends and summarized in Table S5.

1065

1066 **Scientific illustration**

1067 Chemical structures were drawn with ChemDraw Prime. Some parts of Fig. 3a, Fig. 4a,b;
1068 Fig. 6a; and Extended Data Fig. 5a and 10a were created using Biorender.com.

1069

Acknowledgments

We thank Nora Assendorp and Doris Wennagel for their help with *in utero* electroporation; Julie Lefrançois, Mélissa David and Mathilde Murat for their help with cell culture, molecular biology and genotyping; IBENS rodent facility for help with mouse line management; Maria Rodrigo for her help with electrophysiology; Nicolas Delsuc (Chemistry Department, ENS, Paris, France) for training and help on HPLC. The pCAG-GluN2B-IRES-GFP plasmid was a gift from Katherine Roche (NIH, Bethesda, MD, USA). This project was supported by the French Ministry of Research (doctoral fellowship from Ecole Normale Supérieure attributed to A.S.), the European Commission (Marie-Sklodowska-Curie fellowship H2020-MSCA-IF-2015 Grant #701467 to L.M.), the European Research Council (ERC Advanced Grant #693021 to P.P. and ERC starting grant #803704 to C.Ch.), the Fondation pour la Recherche Médicale (FRM) (fellowship no. FDT202304016679 to A.S.), and the French Agence Nationale de la Recherche (ANR JCJC Grant #22-CE16-0016 Opto2B to L.M.).

Author contributions

Compound design and characterization: L.M. and P.P.; molecular biology and *in vitro* electrophysiology: M.T., A.S., Z.M., and L.M.; cell culture: M.T., A.S., and C.Ca.; *in utero* electroporation: J.Z; *ex vivo* electrophysiology on electroporated mice: L.M.; *ex vivo* electrophysiology on Opto2B mice: A.S. and S.S.; mouse line management and genotyping: A.S., C.Ca., and S.S; data analysis: A.S., M.T., S.S, Z.M., P.P. and L.M.; supervision: C.Ch., P.P. and L.M.; design of the project: P.P. and L.M.; acquisition of funding: P.P. and L.M.; writing of the paper: A.S., P.P. and L.M.

Declaration of interests

The authors declare no competing interests

References

1. Smart, T. G. & Paoletti, P. Synaptic Neurotransmitter-Gated Receptors. *Cold Spring Harbor Perspectives in Biology* **4**, a009662–a009662 (2012).
2. Geoffroy, C., Paoletti, P. & Mony, L. Positive allosteric modulation of NMDA receptors: mechanisms, physiological impact and therapeutic potential. *The Journal of Physiology* **600**, 233–259 (2022).
3. Lemoine, D. *et al.* Ligand-Gated Ion Channels: New Insights into Neurological Disorders and Ligand Recognition. *Chem. Rev.* **112**, 6285–6318 (2012).
4. Sente, A. *et al.* Differential assembly diversifies GABAA receptor structures and signalling. *Nature* **604**, 190–194 (2022).
5. Sigel, E. & Steinmann, M. E. Structure, Function, and Modulation of GABAA Receptors. *Journal of Biological Chemistry* **287**, 40224–40231 (2012).
6. Sun, C., Zhu, H., Clark, S. & Gouaux, E. Cryo-EM structures reveal native GABAA receptor assemblies and pharmacology. *Nature* **622**, 195–201 (2023).
7. Hansen, K. B. *et al.* Structure, Function, and Pharmacology of Glutamate Receptor Ion Channels. *Pharmacol Rev* **73**, 1469–1658 (2021).
8. Yu, J. *et al.* Hippocampal AMPA receptor assemblies and mechanism of allosteric inhibition. *Nature* **594**, 448–453 (2021).
9. Zhao, Y., Chen, S., Swensen, A. C., Qian, W.-J. & Gouaux, E. Architecture and subunit arrangement of native AMPA receptors elucidated by cryo-EM. *Science* **364**, 355–362 (2019).
10. Sieghart, W. & Savić, M. M. International Union of Basic and Clinical Pharmacology. CVI: $GABA_A$ Receptor Subtype- and Function-selective Ligands: Key Issues in Translation to Humans. *Pharmacol Rev* **70**, 836–878 (2018).
11. Berlin, S. & Isacoff, E. Y. Synapses in the spotlight with synthetic optogenetics. *EMBO Reports* **18**, 677–692 (2017).
12. Broichhagen, J. & Levitz, J. Advances in tethered photopharmacology for precise optical control of signaling proteins. *Current Opinion in Pharmacology* **63**, 102196 (2022).
13. Hüll, K., Morstein, J. & Trauner, D. *In Vivo* Photopharmacology. *Chem. Rev.* **118**, 10710–10747 (2018).
14. Kramer, R. H., Mourot, A. & Adesnik, H. Optogenetic pharmacology for control of native neuronal signaling proteins. *Nat Neurosci* **16**, 816–823 (2013).
15. Paoletti, P., Ellis-Davies, G. C. R. & Mourot, A. Optical control of neuronal ion channels and receptors. *Nat Rev Neurosci* **20**, 514–532 (2019).
16. Paoletti, P., Bellone, C. & Zhou, Q. NMDA receptor subunit diversity: impact on receptor properties, synaptic plasticity and disease. *Nat Rev Neurosci* **14**, 383–400 (2013).
17. Hanson, J. E. *et al.* Therapeutic potential of N-methyl-D-aspartate receptor modulators in psychiatry. *Neuropsychopharmacol.* **49**, 51–66 (2024).
18. Zhou, Q. & Sheng, M. NMDA receptors in nervous system diseases. *Neuropharmacology* **74**, 69–75 (2013).
19. Sheng, M., Cummings, J., Roldan, L. A., Jan, Y. N. & Jan, L. Y. Changing subunit composition of heteromeric NMDA receptors during development of rat cortex. *Nature* **368**, 144–147 (1994).
20. Stroebel, D., Casado, M. & Paoletti, P. Triheteromeric NMDA receptors: from structure to synaptic physiology. *Curr Opin Physiol* **2**, 1–12 (2018).
21. Dupuis, J. P., Nicole, O. & Groc, L. NMDA receptor functions in health and disease: Old actor, new dimensions. *Neuron* **111**, 2312–2328 (2023).

1142 22. Cui, Z. *et al.* Increased NR2A:NR2B ratio compresses long-term depression range and
1143 constrains long-term memory. *Sci Rep* **3**, 1036 (2013).
1144 23. Sanz-Clemente, A., Nicoll, R. A. & Roche, K. W. Diversity in NMDA receptor
1145 composition: many regulators, many consequences. *Neuroscientist* **19**, 62–75 (2013).
1146 24. Yashiro, K. & Philpot, B. D. Regulation of NMDA receptor subunit expression and its
1147 implications for LTD, LTP, and metaplasticity. *Neuropharmacology* **55**, 1081–1094
1148 (2008).
1149 25. Hansen, K. B., Ogden, K. K., Yuan, H. & Traynelis, S. F. Distinct functional and
1150 pharmacological properties of Triheteromeric GluN1/GluN2A/GluN2B NMDA receptors.
1151 *Neuron* **81**, 1084–1096 (2014).
1152 26. Hatton, C. J. & Paoletti, P. Modulation of triheteromeric NMDA receptors by N-terminal
1153 domain ligands. *Neuron* **46**, 261–274 (2005).
1154 27. Stroebel, D., Carvalho, S., Grand, T., Zhu, S. & Paoletti, P. Controlling NMDA receptor
1155 subunit composition using ectopic retention signals. *J Neurosci* **34**, 16630–16636
1156 (2014).
1157 28. Mony, L., Zhu, S., Carvalho, S. & Paoletti, P. Molecular basis of positive allosteric
1158 modulation of GluN2B NMDA receptors by polyamines. *EMBO J* **30**, 3134–3146 (2011).
1159 29. Williams, K. Modulation and block of ion channels: a new biology of polyamines. *Cell*
1160 *Signal* **9**, 1–13 (1997).
1161 30. Esmenjaud, J.-B. *et al.* An inter-dimer allosteric switch controls NMDA receptor activity.
1162 *EMBO J* **38**, (2019).
1163 31. Tajima, N. *et al.* Activation of NMDA receptors and the mechanism of inhibition by
1164 ifenprodil. *Nature* **534**, 63–68 (2016).
1165 32. Tian, M. *et al.* GluN2A and GluN2B NMDA receptors use distinct allosteric routes. *Nat*
1166 *Commun* **12**, 4709 (2021).
1167 33. Traynelis, S. F., Hartley, M. & Heinemann, S. F. Control of proton sensitivity of the
1168 NMDA receptor by RNA splicing and polyamines. *Science* **268**, 873–876 (1995).
1169 34. Chen, N., Luo, T. & Raymond, L. A. Subtype-dependence of NMDA receptor channel
1170 open probability. *J Neurosci* **19**, 6844–6854 (1999).
1171 35. Blanke, M. L. & VanDongen, A. M. J. Constitutive activation of the N-methyl-D-aspartate
1172 receptor via cleft-spanning disulfide bonds. *J Biol Chem* **283**, 21519–21529 (2008).
1173 36. Gielen, M., Siegler Retchless, B., Mony, L., Johnson, J. W. & Paoletti, P. Mechanism of
1174 differential control of NMDA receptor activity by NR2 subunits. *Nature* **459**, 703–707
1175 (2009).
1176 37. Talukder, I., Borker, P. & Wollmuth, L. P. Specific Sites within the Ligand-Binding
1177 Domain and Ion Channel Linkers Modulate NMDA Receptor Gating. *JOURNAL OF*
1178 *NEUROSCIENCE* **30**, 11792–11804 (2010).
1179 38. Hansen, K. B. *et al.* Structural determinants of agonist efficacy at the glutamate binding
1180 site of N-methyl-D-aspartate receptors. *Mol Pharmacol* **84**, 114–127 (2013).
1181 39. Banghart, M., Borges, K., Isacoff, E., Trauner, D. & Kramer, R. H. Light-activated ion
1182 channels for remote control of neuronal firing. *Nat Neurosci* **7**, 1381–1386 (2004).
1183 40. Berlin, S. *et al.* A family of photoswitchable NMDA receptors. *eLife* **5**, e12040 (2016).
1184 41. Durand-de Cuttoli, R. *et al.* Manipulating midbrain dopamine neurons and reward-
1185 related behaviors with light-controllable nicotinic acetylcholine receptors. *eLife* **7**,
1186 e37487 (2018).
1187 42. Levitz, J. *et al.* Optical control of metabotropic glutamate receptors. *Nat Neurosci* **16**,
1188 507–516 (2013).

1189 43. Lin, W.-C. *et al.* A Comprehensive Optogenetic Pharmacology Toolkit for In Vivo Control
1190 of GABAA Receptors and Synaptic Inhibition. *Neuron* **88**, 879–891 (2015).
1191 44. Zhu, S. & Paoletti, P. Allosteric modulators of NMDA receptors: multiple sites and
1192 mechanisms. *Curr Opin Pharmacol* **20**, 14–23 (2015).
1193 45. Hansen, K. B. *et al.* Structure, function, and allosteric modulation of NMDA receptors.
1194 *Journal of General Physiology* **150**, 1081–1105 (2018).
1195 46. Williams, K., Zappia, A. M., Pritchett, D. B., Shen, Y. M. & Molinoff, P. B. Sensitivity of
1196 the N-methyl-D-aspartate receptor to polyamines is controlled by NR2 subunits. *Mol*
1197 *Pharmacol* **45**, 803–809 (1994).
1198 47. Fossati, M. *et al.* Trans-Synaptic Signaling through the Glutamate Receptor Delta-1
1199 Mediates Inhibitory Synapse Formation in Cortical Pyramidal Neurons. *Neuron* **104**,
1200 1081-1094.e7 (2019).
1201 48. Meyer-Dilhet, G. & Courchet, J. In Utero Cortical Electroporation of Plasmids in the
1202 Mouse Embryo. *STAR Protoc* **1**, 100027 (2020).
1203 49. Meur, K. L., Galante, M., Angulo, M. C. & Audinat, E. Tonic activation of NMDA
1204 receptors by ambient glutamate of non-synaptic origin in the rat hippocampus. *J Physiol*
1205 **580**, 373–383 (2007).
1206 50. Papouin, T. *et al.* Synaptic and extrasynaptic NMDA receptors are gated by different
1207 endogenous coagonists. *Cell* **150**, 633–646 (2012).
1208 51. Papouin, T. & Oliet, S. H. R. Organization, control and function of extrasynaptic NMDA
1209 receptors. *Philos Trans R Soc Lond B Biol Sci* **369**, 20130601 (2014).
1210 52. Sah, P., Hestrin, S. & Nicoll, R. A. Tonic activation of NMDA receptors by ambient
1211 glutamate enhances excitability of neurons. *Science* **246**, 815–818 (1989).
1212 53. Wu, Y.-W., Grebenyuk, S., McHugh, T. J., Rusakov, D. A. & Semyanov, A.
1213 Backpropagating Action Potentials Enable Detection of Extrasynaptic Glutamate by
1214 NMDA Receptors. *Cell Reports* **1**, 495–505 (2012).
1215 54. Williams, K. Mechanisms influencing stimulatory effects of spermine at recombinant N-
1216 methyl-D-aspartate receptors. *Mol Pharmacol* **46**, 161–168 (1994).
1217 55. Kalivas, P. Extracellular Glutamate: Functional Compartments Operate in Different
1218 Concentration Ranges. *Front. Syst. Neurosci.* **5**, (2011).
1219 56. Herman, M. A. & Jahr, C. E. Extracellular Glutamate Concentration in Hippocampal
1220 Slice. *J. Neurosci.* **27**, 9736–9741 (2007).
1221 57. Moldavski, A., Behr, J., Bading, H. & Bengtson, C. P. A novel method using ambient
1222 glutamate for the electrophysiological quantification of extrasynaptic NMDA receptor
1223 function in acute brain slices. *The Journal of Physiology* **598**, 633–650 (2020).
1224 58. Parsons, M. P. & Raymond, L. A. Extrasynaptic NMDA receptor involvement in central
1225 nervous system disorders. *Neuron* **82**, 279–293 (2014).
1226 59. Kew, J. N., Trube, G. & Kemp, J. A. A novel mechanism of activity-dependent NMDA
1227 receptor antagonism describes the effect of ifenprodil in rat cultured cortical neurones.
1228 *The Journal of Physiology* **497**, 761–772 (1996).
1229 60. Akazawa, C., Shigemoto, R., Bessho, Y., Nakanishi, S. & Mizuno, N. Differential
1230 expression of five N-methyl-D-aspartate receptor subunit mRNAs in the cerebellum of
1231 developing and adult rats. *J Comp Neurol* **347**, 150–160 (1994).
1232 61. Monyer, H., Burnashev, N., Laurie, D. J., Sakmann, B. & Seeburg, P. H. Developmental
1233 and regional expression in the rat brain and functional properties of four NMDA
1234 receptors. *Neuron* **12**, 529–540 (1994).

62. Watanabe, M., Inoue, Y., Sakimura, K. & Mishina, M. Distinct distributions of five N-methyl-D-aspartate receptor channel subunit mRNAs in the forebrain. *J Comp Neurol* **338**, 377–390 (1993).
63. Hardingham, G. E. & Bading, H. Synaptic versus extrasynaptic NMDA receptor signalling: implications for neurodegenerative disorders. *Nat Rev Neurosci* **11**, 682–696 (2010).
64. Köhr, G. NMDA receptor function: subunit composition versus spatial distribution. *Cell Tissue Res* **326**, 439–446 (2006).
65. Gladding, C. M. & Raymond, L. A. Mechanisms underlying NMDA receptor synaptic/extrasynaptic distribution and function. *Mol Cell Neurosci* **48**, 308–320 (2011).
66. Sakimura, K. *et al.* Reduced hippocampal LTP and spatial learning in mice lacking NMDA receptor ε1 subunit. *Nature* **373**, 151–155 (1995).
67. Bellone, C. & Nicoll, R. A. Rapid bidirectional switching of synaptic NMDA receptors. *Neuron* **55**, 779–785 (2007).
68. Ferreira, J. S. *et al.* Co-agonists differentially tune GluN2B-NMDA receptor trafficking at hippocampal synapses. *Elife* **6**, (2017).
69. Belkacemi, K., Rondard, P., Pin, J.-P. & Prézeau, L. Heterodimers Revolutionize the Field of Metabotropic Glutamate Receptors. *Neuroscience* (2024) doi:10.1016/j.neuroscience.2024.06.013.
70. DeDominicis, K. E. *et al.* The (α4)3(β2)2 Stoichiometry of the Nicotinic Acetylcholine Receptor Predominates in the Rat Motor Cortex. *Mol Pharmacol* **92**, 327–337 (2017).
71. Meng, J. *et al.* Nanobody-based sensors reveal a high proportion of mGlu heterodimers in the brain. *Nat Chem Biol* **18**, 894–903 (2022).
72. Bettini, E. *et al.* Identification and characterization of novel NMDA receptor antagonists selective for NR2A- over NR2B-containing receptors. *J Pharmacol Exp Ther* **335**, 636–644 (2010).
73. Volkmann, R. A. *et al.* MPX-004 and MPX-007: New Pharmacological Tools to Study the Physiology of NMDA Receptors Containing the GluN2A Subunit. *PLoS One* **11**, e0148129 (2016).
74. Hackos, D. H. *et al.* Positive Allosteric Modulators of GluN2A-Containing NMDARs with Distinct Modes of Action and Impacts on Circuit Function. *Neuron* **89**, 983–999 (2016).
75. Yi, F. *et al.* Structural Basis for Negative Allosteric Modulation of GluN2A-Containing NMDA Receptors. *Neuron* **91**, 1316–1329 (2016).
76. Cheriyan, J., Balsara, R. D., Hansen, K. B. & Castellino, F. J. Pharmacology of triheteromeric N-Methyl-d-Aspartate Receptors. *Neuroscience Letters* **617**, 240–246 (2016).
77. Mony, L., Kew, J. N., Gunthorpe, M. J. & Paoletti, P. Allosteric modulators of NR2B-containing NMDA receptors: molecular mechanisms and therapeutic potential. *Br J Pharmacol* **157**, 1301–1317 (2009).
78. Yi, F., Bhattacharya, S., Thompson, C. M., Traynelis, S. F. & Hansen, K. B. Functional and pharmacological properties of triheteromeric GluN1/2B/2D NMDA receptors. *J Physiol* **597**, 5495–5514 (2019).
79. Zheng, F. *et al.* Allosteric interaction between the amino terminal domain and the ligand binding domain of NR2A. *Nat Neurosci* **4**, 894–901 (2001).
80. Paoletti, P., Ascher, P. & Neyton, J. High-affinity zinc inhibition of NMDA NR1-NR2A receptors. *J Neurosci* **17**, 5711–5725 (1997).

1281 81. Gray, J. A. *et al.* Distinct Modes of AMPA Receptor Suppression at Developing
1282 Synapses by GluN2A and GluN2B: Single-Cell NMDA Receptor Subunit Deletion
1283 In Vivo. *Neuron* **71**, 1085–1101 (2011).
1284 82. Al-Hallaq, R. A., Conrads, T. P., Veenstra, T. D. & Wenthold, R. J. NMDA Di-Heteromeric
1285 Receptor Populations and Associated Proteins in Rat Hippocampus. *J. Neurosci.* **27**,
1286 8334–8343 (2007).
1287 83. Chazot, P. L. & Stephenson, F. A. Molecular Dissection of Native Mammalian Forebrain
1288 NMDA Receptors Containing the NR1 C2 Exon: Direct Demonstration of NMDA
1289 Receptors Comprising NR1, NR2A, and NR2B Subunits Within the Same Complex.
1290 *Journal of Neurochemistry* **69**, 2138–2144 (1997).
1291 84. Luo, J., Wang, Y., Yasuda, R. P., Dunah, A. W. & Wolfe, B. B. The Majority of *N* -Methyl-
1292 d-Aspartate Receptor Complexes in Adult Rat Cerebral Cortex Contain at Least Three
1293 Different Subunits (NR1/NR2A/NR2B). *Mol Pharmacol* **51**, 79–86 (1997).
1294 85. Rauner, C. & Köhr, G. Triheteromeric NR1/NR2A/NR2B receptors constitute the major
1295 N-methyl-D-aspartate receptor population in adult hippocampal synapses. *J Biol Chem*
1296 **286**, 7558–7566 (2011).
1297 86. Tovar, K. R., McGinley, M. J. & Westbrook, G. L. Triheteromeric NMDA receptors at
1298 hippocampal synapses. *J Neurosci* **33**, 9150–9160 (2013).
1299 87. Kellermayer, B. *et al.* Differential Nanoscale Topography and Functional Role of GluN2-
1300 NMDA Receptor Subtypes at Glutamatergic Synapses. *Neuron* **100**, 106-119.e7 (2018).
1301 88. von Engelhardt, J. *et al.* GluN2D-containing NMDA receptors-mediate synaptic currents
1302 in hippocampal interneurons and pyramidal cells in juvenile mice. *Front. Cell. Neurosci.*
1303 **9**, (2015).
1304 89. Fellin, T. *et al.* Neuronal synchrony mediated by astrocytic glutamate through activation
1305 of extrasynaptic NMDA receptors. *Neuron* **43**, 729–743 (2004).
1306 90. Scimemi, A., Fine, A., Kullmann, D. M. & Rusakov, D. A. NR2B-Containing Receptors
1307 Mediate Cross Talk among Hippocampal Synapses. *J. Neurosci.* **24**, 4767–4777 (2004).
1308 91. Tovar, K. R. & Westbrook, G. L. The Incorporation of NMDA Receptors with a Distinct
1309 Subunit Composition at Nascent Hippocampal Synapses *In Vitro*. *J. Neurosci.* **19**,
1310 4180–4188 (1999).
1311 92. Harris, A. Z. & Pettit, D. L. Extrasynaptic and synaptic NMDA receptors form stable and
1312 uniform pools in rat hippocampal slices. *The Journal of Physiology* **584**, 509–519
1313 (2007).
1314 93. Le Meur, K., Galante, M., Angulo, M. C. & Audinat, E. Tonic activation of NMDA
1315 receptors by ambient glutamate of non-synaptic origin in the rat hippocampus. *J Physiol*
1316 **580**, 373–383 (2007).
1317 94. Mohrmann, R., Hatt, H. & Gottmann, K. Developmental regulation of subunit
1318 composition of extrasynaptic NMDA receptors in neocortical neurones: *NeuroReport* **11**,
1319 1203–1208 (2000).
1320 95. Petralia, R. S. *et al.* Organization of NMDA receptors at extrasynaptic locations.
1321 *Neuroscience* **167**, 68–87 (2010).
1322 96. Paoletti, P., Neyton, J. & Ascher, P. Glycine-independent and subunit-specific
1323 potentiation of NMDA responses by extracellular Mg2+. *Neuron* **15**, 1109–1120 (1995).
1324 97. Igarashi, K., Shirahata, A., Pahk, A. J., Kashiwagi, K. & Williams, K. Benzyl-polyamines:
1325 novel, potent N-methyl-D-aspartate receptor antagonists. *J Pharmacol Exp Ther* **283**,
1326 533–540 (1997).
1327 98. Kashiwagi, K., Pahk, A. J., Masuko, T., Igarashi, K. & Williams, K. Block and modulation
1328 of N-methyl-D-aspartate receptors by polyamines and protons: role of amino acid

residues in the transmembrane and pore-forming regions of NR1 and NR2 subunits. *Mol Pharmacol* **52**, 701–713 (1997).

99. Gielen, M. *et al.* Structural rearrangements of NR1/NR2A NMDA receptors during allosteric inhibition. *Neuron* **57**, 80–93 (2008).
100. von Engelhardt, J. *et al.* Contribution of hippocampal and extra-hippocampal NR2B-containing NMDA receptors to performance on spatial learning tasks. *Neuron* **60**, 846–860 (2008).
101. Yan, J., Bengtson, C. P., Buchthal, B., Hagenston, A. M. & Bading, H. Coupling of NMDA receptors and TRPM4 guides discovery of unconventional neuroprotectants. *Science* (2020) doi:10.1126/science.aay3302.
102. Hunter, J. D. Matplotlib: A 2D Graphics Environment. *Computing in Science & Engineering* **9**, 90–95 (2007).
103. Waskom, M. seaborn: statistical data visualization. *JOSS* **6**, 3021 (2021).

Main Figures

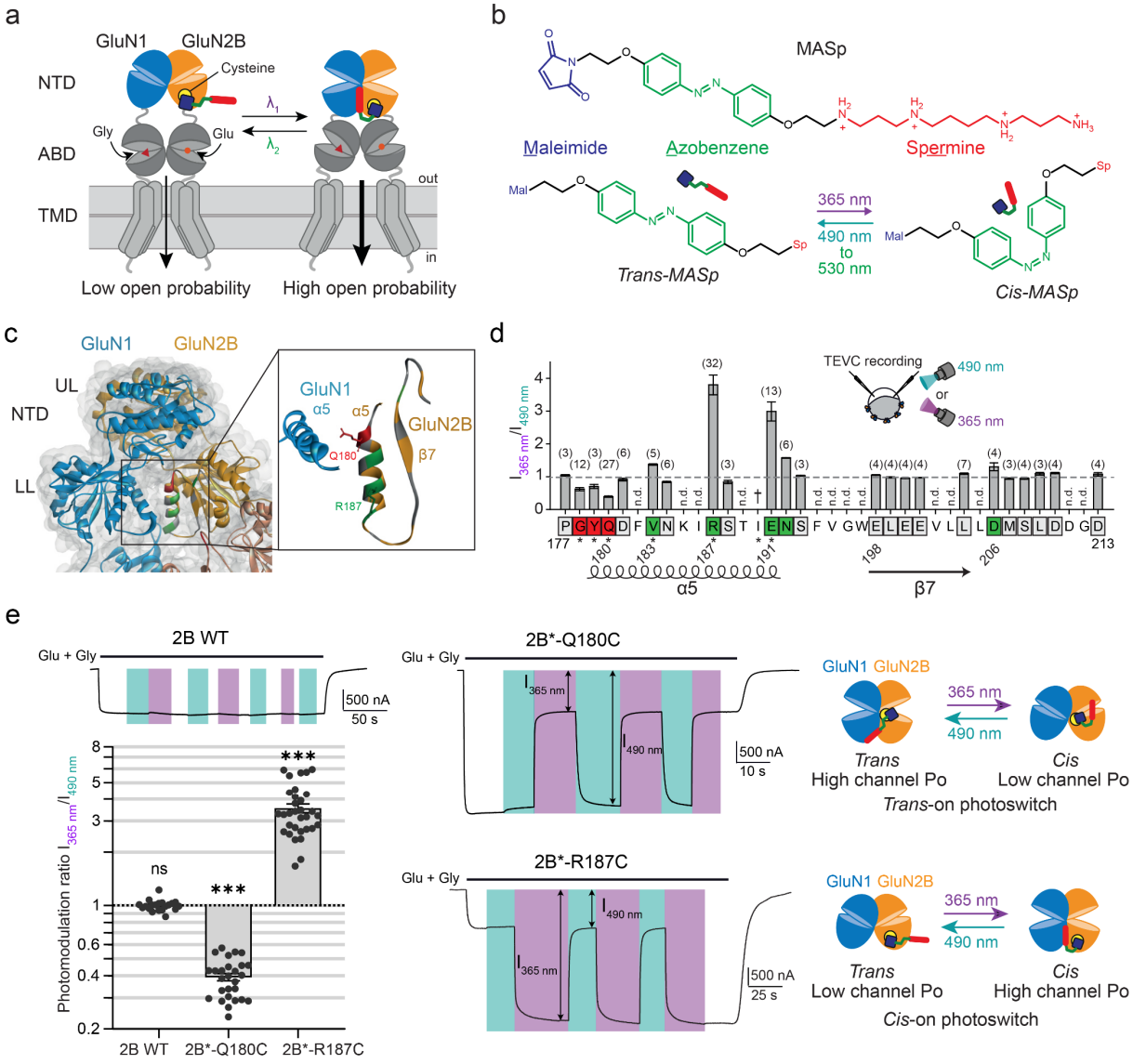

Fig. 1: Engineering light-sensitive GluN2B-NMDARs. (a) Schematic of a dimer of GluN1 and GluN2B subunits. GluN1 and GluN2B NTDs are colored in blue and orange, respectively. To photo-enhance GluN2B-NMDAR activity, the idea is to introduce a photoswitchable polyamine derivative in proximity of the polyamine positive allosteric modulation site, at the interface between the lower lobes of GluN1 and GluN2B NTDs[28]. **(b)** Chemical structure of MASp, a photoswitchable spermine derivative, in its *trans* and *cis* configurations. **(c-d)** Screening for MASp labeling positions yielding photomodulation. **(c)** Left, X-ray structure of an NTD dimer in its "active" form (pdb 5FXG[31]) with the positions tested for photomodulation highlighted on the GluN2B subunit. Right, close-up view of the NTD lower lobe - lower lobe interface. Positions were screened along the α5 helix and β7 strand of the NTD of the GluN2B subunit. Screened labeling positions are color-coded as follows: grey, positions yielding no or little (< 30%) photomodulation of MASp-labeled

1357 GluN1/GluN2B; red, positions for which UV light induces an inhibition > 30%; green,
1358 positions for which UV light induces a potentiation > 30% (see **d**). UL, upper lobe; LL, lower
1359 lobe. **(d)** Summary of the amount of photomodulation (expressed as the current ratio
1360 between 365 and 490 nm light) obtained on NMDARs containing a GluN2B subunit mutated
1361 with a cysteine at the shown positions and labeled with MASp. For each position, the number
1362 of oocytes tested is indicated in parenthesis. n.d., not tested; †, no expression of the cysteine
1363 mutant; *, the cysteine mutation was made on the GluN2B-C395S background. Same color
1364 code as in **c**. **(e)** Current traces from oocytes expressing GluN1/GluN2B WT, GluN1/GluN2B-
1365 Q180C-C395S (2B*-Q180C) or GluN1/GluN2B-R187C-C395S (2B*-R187C) receptors
1366 following application of glutamate (Glu) and glycine (Gly) (100 μM each) and under
1367 illumination with 365 (violet bars) or 490 nm light (blue-green bars), and summary of the
1368 photomodulation ratios ($I_{365\ nm}/I_{490\ nm}$) for these three constructs. Right, proposed mechanism
1369 of MASp light-dependent action when bound to Q180C (top) or R187C (bottom) (see
1370 Extended Data Fig. 2a,b). n.s., $p > 0.05$; ***, $p < 0.001$; multiple one sample Wilcoxon tests
1371 against the value 1, p-values were adjusted for multiple comparisons using Bonferroni
1372 correction. All recordings were performed at pH6.5. Values and cell numbers are described in
1373 Supplementary Table 1.

1374

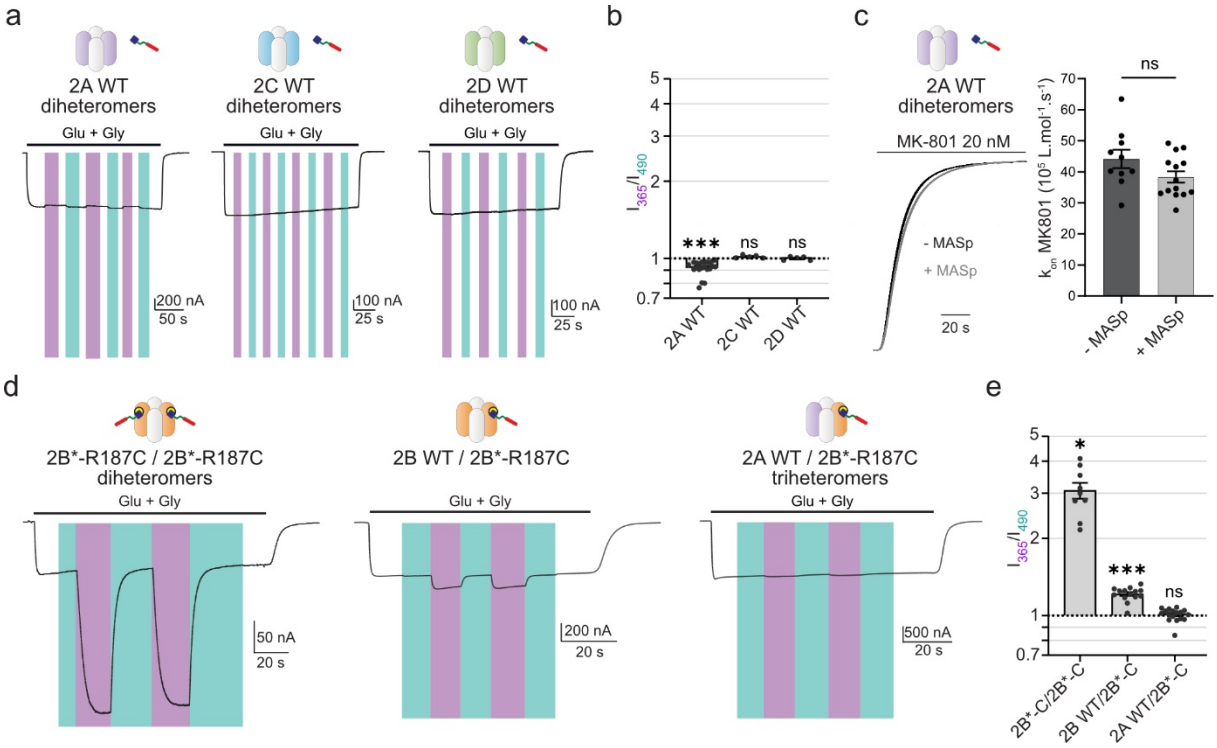

Fig. 2: Selective photomodulation of GluN2B diheteromers. (a-c) MASp labeling induces no or little photodependent effect on the function of GluN2A, GluN2C and GluN2D diheteromers. **(a)** Current trace from a MASp-labeled Xenopus oocyte expressing GluN1/GluN2A, GluN1/GluN2C or GluN1/GluN2D NMDARs upon perfusion of agonists glutamate (Glu) and glycine (Gly) (100 µM each) and submitted to illumination with 365 nm (violet bars) or 490 nm light (blue-green bars). **(b)** Summary of photomodulation ratios ($I_{365\ nm}/I_{490\ nm}$). n.s., $p > 0.05$; ***, $p < 0.001$; one sample Wilcoxon test, p-values were adjusted for multiple comparisons using Bonferroni correction. **(c)** Left, superposed MK-801 inhibition traces of unlabeled (- MASp, black) and labeled (+ MASp, grey) WT GluN1/GluN2A NMDARs kept in the dark (MASp in its *trans* state). Right, MK-801 inhibition rates of unlabeled and labeled WT GluN1/GluN2A NMDARs. ns, $p > 0.05$, Mann-Whitney test. **(d)** Current traces from Xenopus oocytes expressing NMDARs with defined subunit stoichiometry using the retention signal strategy described in ref [27], and labeled with MASp, following perfusion of agonists (glutamate and glycine, 100 µM each) under 365 or 490 nm illumination: GluN1/GluN2B*-R187C-r1/GluN2B*-R187C-r2 diheteromer (left), GluN1/GluN2Bwt-r1/GluN2B*-R187C-r2 (middle) and GluN1/GluN2Awt-r1/GluN2B*-R187C-r2 (right) triheteromers. **(e)** Summary of the photomodulation ratios ($I_{365\ nm}/I_{490\ nm}$) for the different constructs. n.s., $p > 0.05$; *, $p < 0.05$; ***, $p < 0.001$; multiple one sample Wilcoxon tests against the value 1, p-values were adjusted for multiple comparisons using Bonferroni correction. All recordings were performed at pH6.5. Photomodulation values and cell numbers are summarized in Supplementary Table 1.

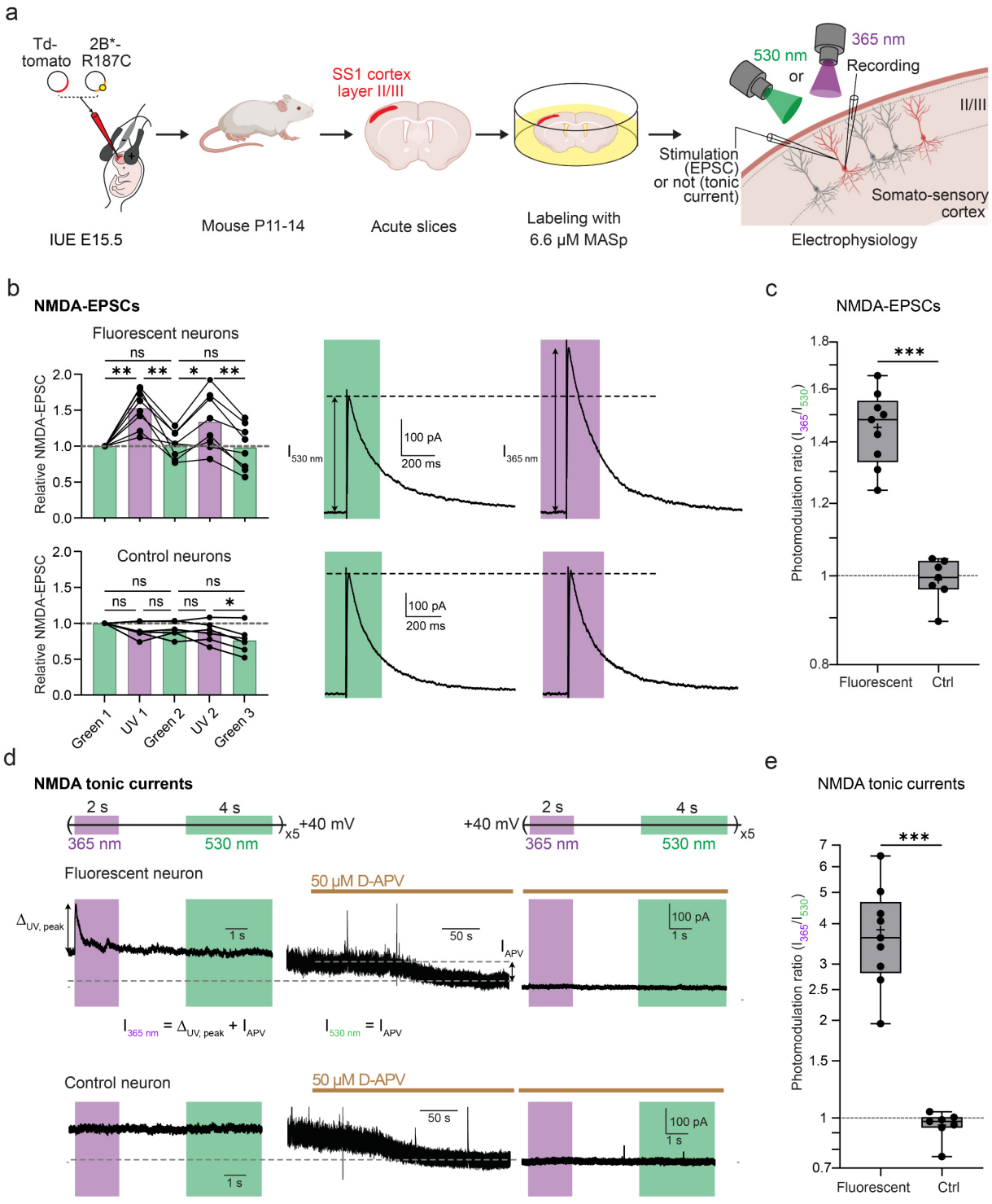

Fig. 3: Photocontrol of NMDA synaptic and tonic currents in brain slices. (a) Experimental workflow for *in vivo* expression of GluN2B*-R187C and *ex-vivo* photomodulation of currents from GluN2B diheteromers. See Main Text and Methods for more details. **(b,c)** Photocontrol of NMDA-EPSCs. **(b)** Left, NMDA-EPSC amplitudes of MASp-labeled, fluorescent (i.e. electroporated, top) and non-fluorescent (control, bottom) neurons from P11-14 mice during alternating cycles of 530 nm (green bars) and 365 nm light (violet bars), normalized to the amplitude of the first set of EPSCs under green light. Each

1405 dot represents the average amplitude of 3 NMDA-EPSCs for each illumination cycle for each
1406 cell (see Extended Data Fig. 5b). n.s., $p > 0.05$; * $p < 0.05$; **, $p < 0.01$, Repeated-measures
1407 Anova followed by Tukey's multiple comparison test. Right, representative NMDA-EPSCs
1408 from a fluorescent (top) and a control (non-fluorescent, bottom) neuron. These traces are the
1409 average EPSC traces over three bouts of illumination (9 EPSCs in total) for the 530 nm light
1410 condition, and over two bouts of illumination (6 EPSCs in total) for the 365 nm light condition
1411 (see Extended Data Fig. 5b and Methods for the photostimulation protocol). **(c)** NMDA-EPSC
1412 photomodulation ratios (calculated as the average NMDA-EPSC amplitudes in 365 nm light
1413 over the average NMDA-EPSC amplitudes in 530 nm light) of MASp-labeled, fluorescent and
1414 control cortical neurons from P11-14 mice. Photomodulation values and cell numbers are
1415 summarized in Supplementary Table 3. ***, $p < 0.001$, Mann-Whitney test. **(d,e)** Photocontrol
1416 of NMDA tonic currents. **(d)** Top, protocol of tonic current photomodulation (no electrical
1417 stimulation). Bottom, tonic current traces of MASp-labeled, fluorescent and control (non-
1418 fluorescent) neurons from a P13 animal before (left) and during (middle and right) application
1419 of 50 μM D-APV. Left and right traces are the average of 5 traces. Arrows indicate the
1420 currents measured to calculate the photomodulation ratio. **(e)** Photomodulation ratios
1421 (calculated as $I_{365\ nm}/I_{530\ nm}$) of NMDA tonic currents of MASp-labeled, fluorescent and control
1422 neurons from P11-P14 animals. ***, $p < 0.001$, Mann-Whitney test. All recordings in brain
1423 slices were performed at physiological pH. Photomodulation values and cell numbers are
1424 summarized in Supplementary Table 3.

1425

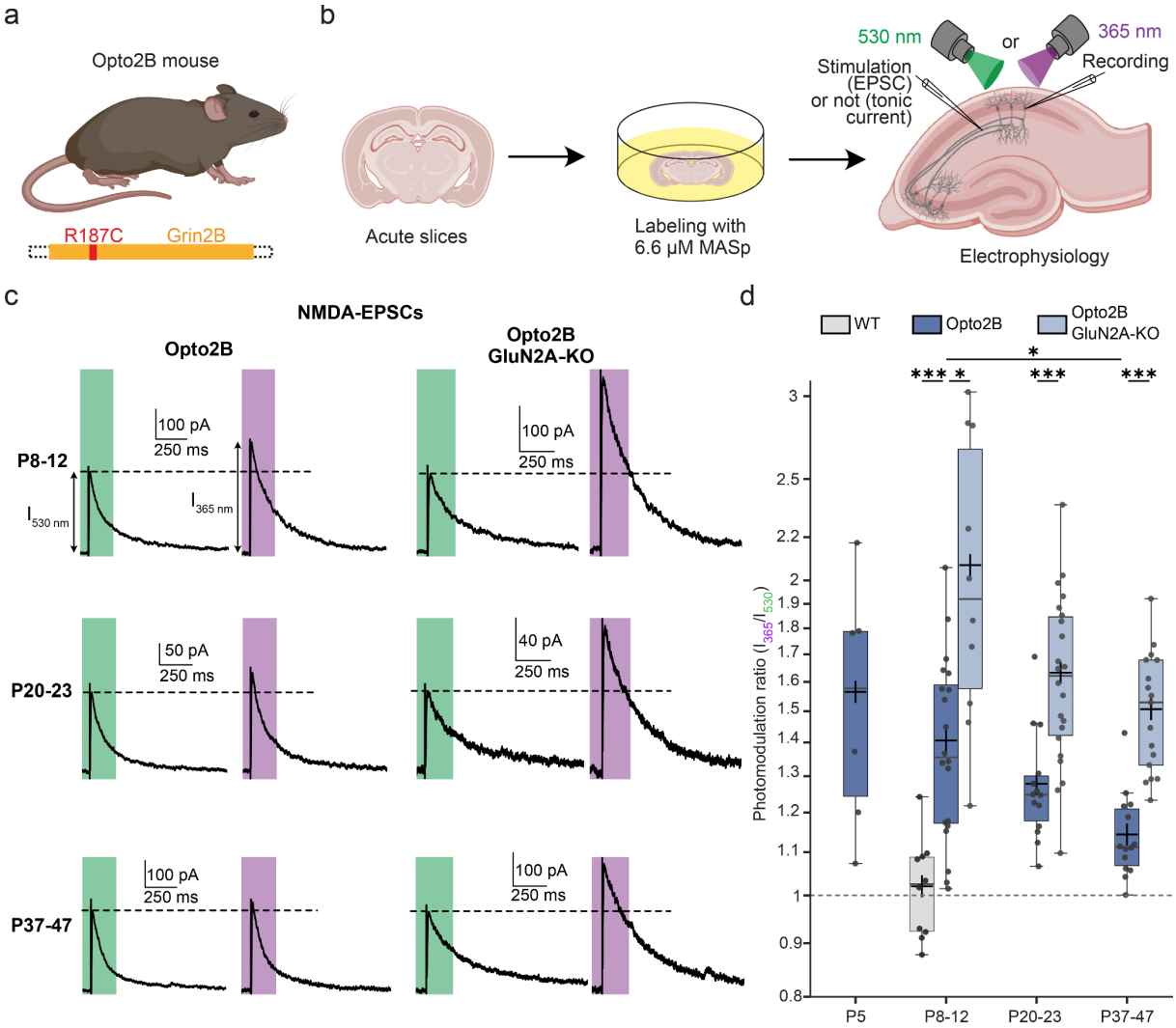

1426

1427 **Fig. 4: Optical profiling of NMDAR subtypes at CA3-CA1 synaptic sites. (a)** Generation
1428 of a KI mouse endogenously expressing GluN2B-R187C (Opto2B mouse). **(b)** Experimental
1429 workflow for *ex-vivo* photomodulation of GluN2B diheteromers at the CA3-CA1 synapse of
1430 the hippocampus. See Main Text and Methods for more details. **(c)** Representative NMDA-
1431 EPSCs of MASp-labeled, CA1 pyramidal neurons from Opto2B (left) or Opto2B/GluN2A-KO
1432 (right) mice at different age ranges (P8-P12, top; P20-P23, middle; P37-P47, bottom) under
1433 530 nm (green bars) and 365 nm light (violet bars). These traces are the average EPSC
1434 traces over two bouts of illumination (6 EPSCs in total) for the 530 nm light condition and
1435 over one bout of illumination (3 EPSCs in total) for the 365 nm light condition, which is
1436 sandwiched between the two previous ones (green – UV – green cycle, see Methods). **(d)**
1437 Summary of NMDA-EPSC photomodulation ratios for MASp-labeled, CA1 pyramidal neurons
1438 from WT (grey), Opto2B (dark blue) and Opto2B/GluN2A-KO (light blue) mice at different age
1439 ranges. All recordings in brain slices were performed at physiological pH. Photomodulation
1440 values and cell numbers are summarized in Supplementary Table 4. *, $p < 0.05$; **, $p < 0.01$;

1441 ***, $p < 0.001$; multiple Mann-Whitney tests; p-values were adjusted for multiple comparisons
1442 using Bonferroni correction. Only the indicated comparisons were performed.

1443

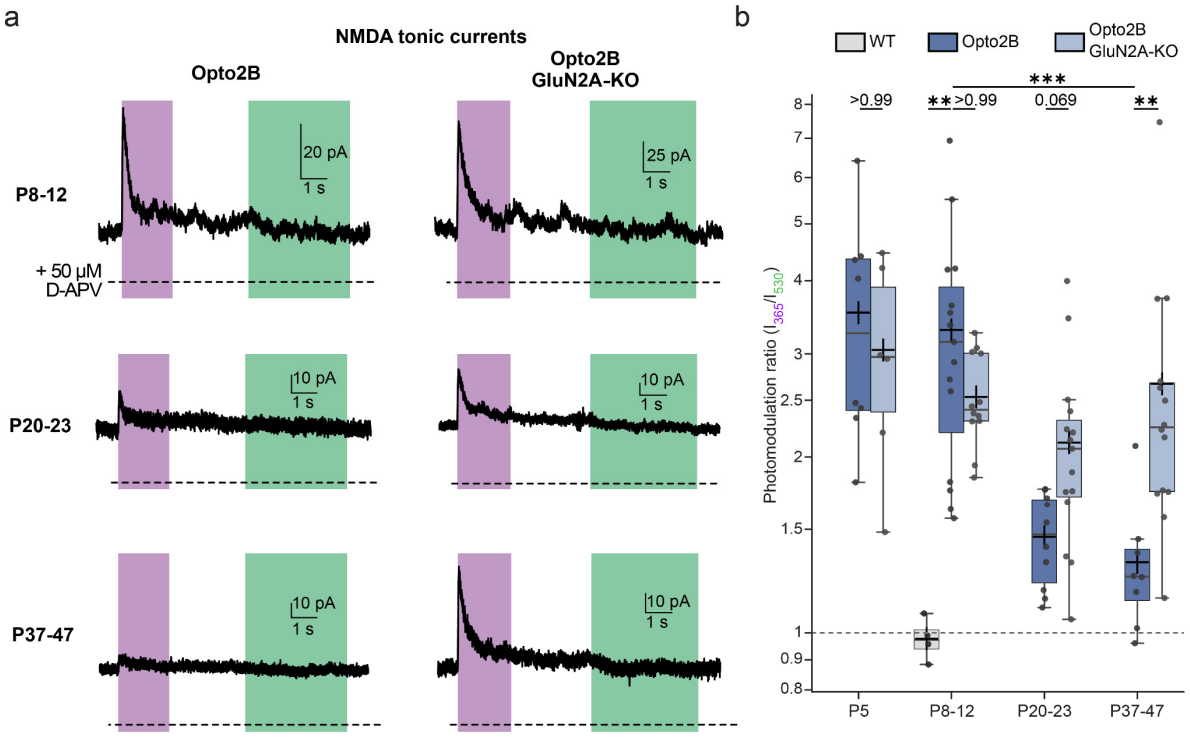

Fig. 5: Optical profiling of NMDAR subtypes at CA1 extrasynaptic sites. (a) Representative tonic NMDA current traces of MASp-labeled, CA1 pyramidal neurons from Opto2B (left) or Opto2B/GluN2A-KO (right) mice at different age ranges (P8-P12, top; P20-P23, middle; P37-P47, bottom) under illumination by 365 nm (violet bars) and 530 nm light (green bars). The dotted line shows the level of tonic current under application of 50 µM D-APV (as in Extended Data Fig. 10b). Tonic current traces are the averages of 5 to 10 traces. **(b)** Summary of the photomodulation ratios of NMDA tonic currents of MASp-labeled, CA1 pyramidal neurons from WT (grey), Opto2B (dark blue) and Opto2B GluN2A-KO (light blue) mice at different age ranges. All recordings in brain slices were performed at physiological pH. Photomodulation values and cell numbers are summarized in Supplementary Table 4. For non-significant p-values, p-values are indicated directly in the graph. **, $p < 0.01$;***, $p < 0.001$; multiple Mann-Whitney tests, p-values were adjusted for multiple comparisons using Bonferroni correction. Only the indicated comparisons were performed.

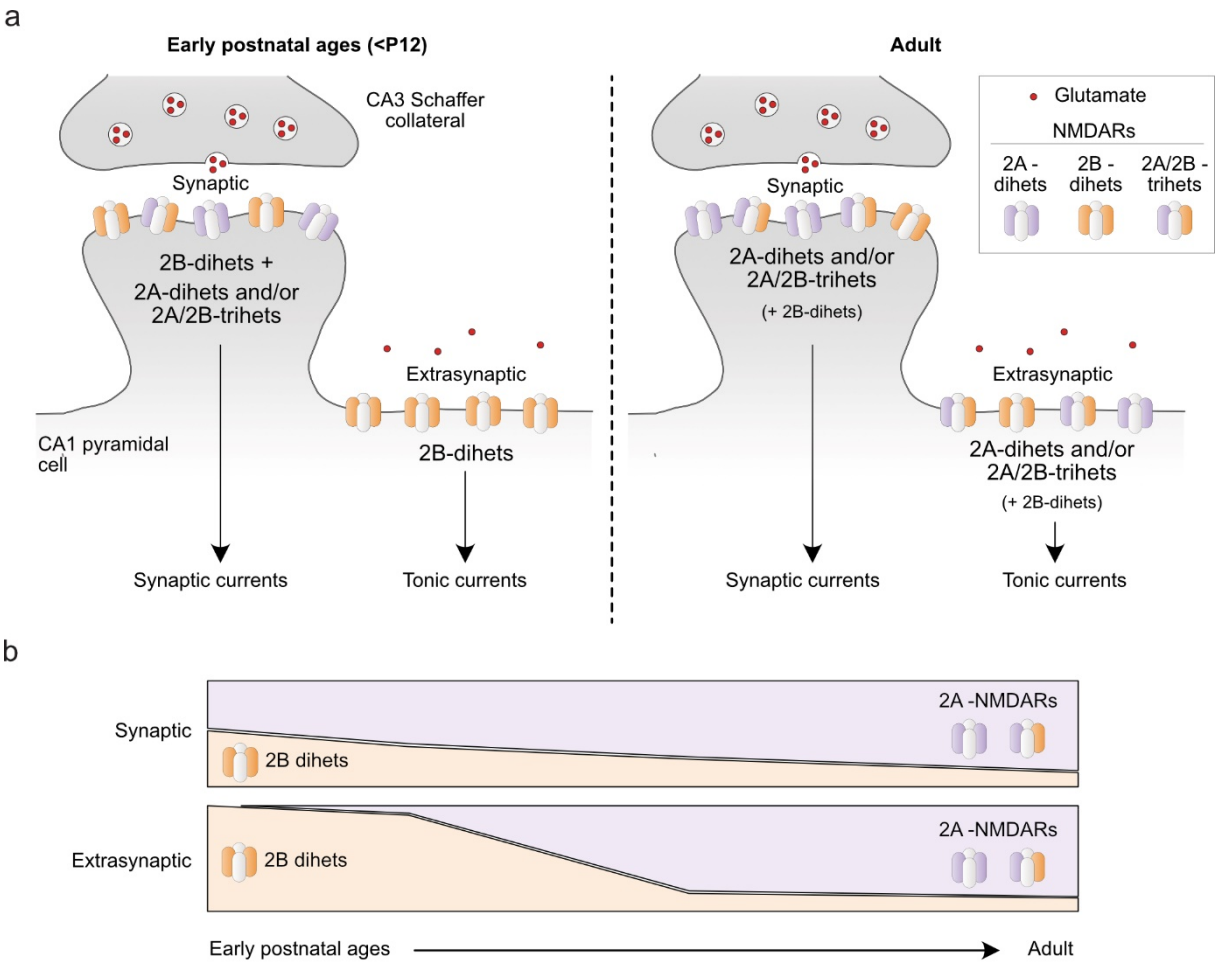

Figure 6: Model of developmental regulation of synaptic and extrasynaptic NMDARs in CA1 pyramidal cells. (a) Left, at early postnatal ages, GluN2B diheteromers are present at the synapse together with GluN2A-NMDARs (GluN2A diheteromers and/or GluN2A/GluN2B triheteromers). On the contrary, extrasynaptic NMDARs are mainly composed of GluN2B diheteromers. Right, in adolescent and adult mice, GluN2A-NMDARs form the major NMDAR populations at both synaptic and extrasynaptic sites. **(b)** Qualitative model of the evolution of the relative abundance of synaptic (top) and extrasynaptic (bottom) GluN2B diheteromers and GluN2A-NMDARs (GluN2A diheteromers and GluN2A/GluN2B triheteromers) across development.

1470 # Extended Data Figures

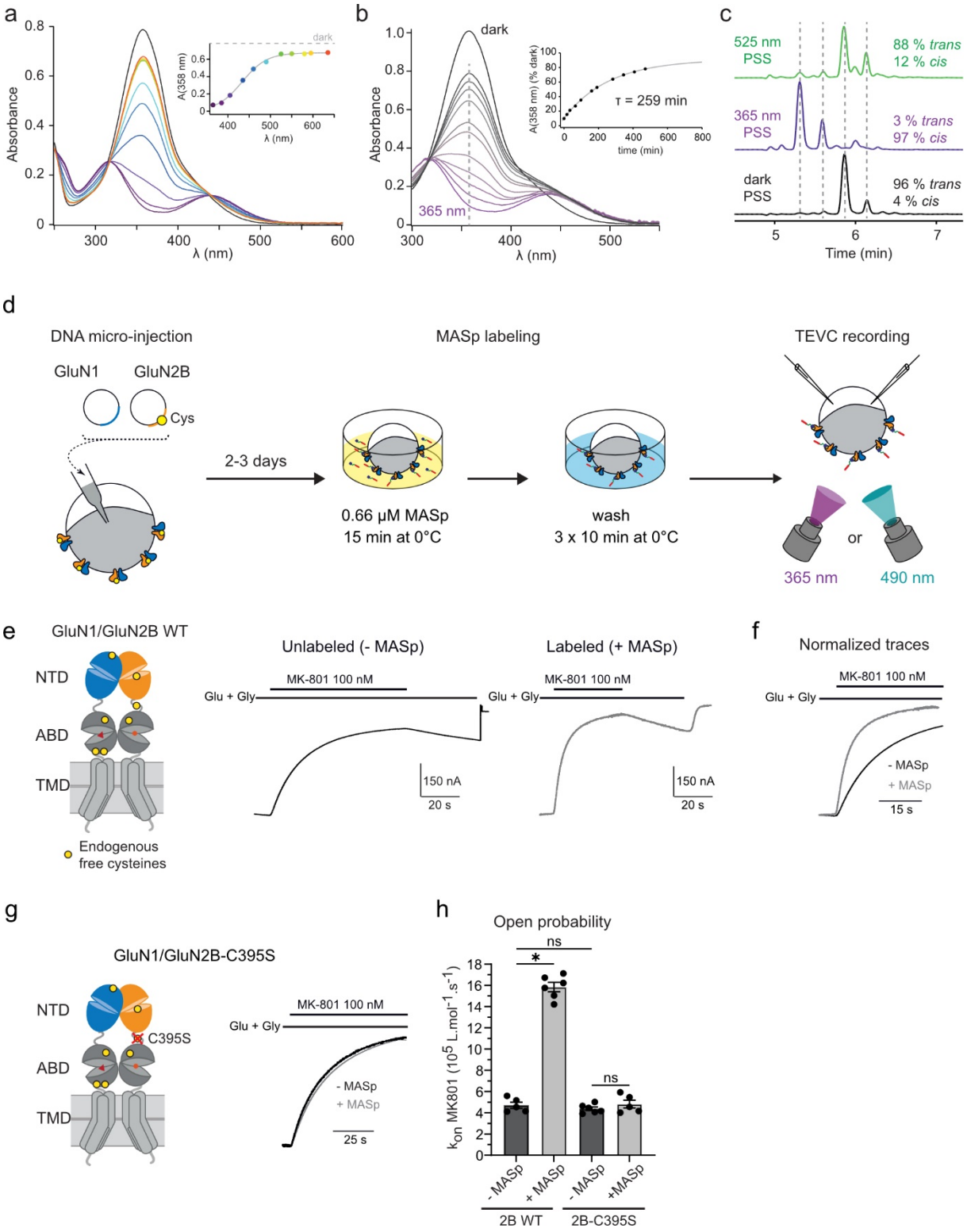

1471

1472 **Extended Data Fig. 1 (related to Fig. 1): Photochemical properties of MASp and design**
1473 **of the labeling conditions in Xenopus oocytes.**

1474 **(a)** UV-visible spectra of MASp conjugated to L-cysteine ($MASp_{Cys}$, see Methods and
1475 Supplementary Fig. 1) in oocyte recording medium (pH 7.3, 33 μM MASp) in the dark (black
1476 trace) and under illumination with increasing wavelengths, from 365 nm (dark violet) to
1477 635 nm (red). Inset, absorbance at 358 nm (*trans*-$MASp_{Cys}$ absorbance peak) as a function
1478 of the illumination wavelength. **(b)** Thermal stability of *cis*-$MASp_{Cys}$. After recording a UV-
1479 visible spectrum of $MASp_{Cys}$ in the dark (mainly *trans* state, black trace), $MASp_{Cys}$ was
1480 irradiated for 10 min by 365 nm light to yield mainly *cis*-$MASp_{Cys}$ (violet spectrum). Spectra in
1481 violet/grey gradation represent the gradual *cis*-to-*trans* transition of $MASp_{Cys}$ in the dark at
1482 different time points (up to ~8 h) post UV irradiation. Inset, evolution over time of the
1483 absorbance at 358 nm. Single-exponential fit (grey line) yielded a time constant τ = 259 min
1484 (~4 h) for *cis*-to-*trans* $MASp_{Cys}$ thermal relaxation in the dark. **(c)** HPLC chromatograms
1485 monitored at the isosbestic point (440 nm) of the photostationary states (PSS) of $MASp_{Cys}$ in
1486 the dark (black trace), after illumination with 365 nm light (violet trace) and subsequent
1487 illumination with 525 nm light (green trace). **(d)** Experimental workflow for heterologous
1488 expression of GluN1/GluN2B receptors, MASp labeling and photomodulation of NMDAR
1489 activity in Xenopus oocytes. **(e-h)** MASP binds to the endogenous cysteine GluN2B-C395.
1490 **(e)** Left, schematic of a GluN1/GluN2B dimer with the positions of the free cysteines (i.e. not
1491 involved in disulfide bridges) highlighted in yellow. Right, inhibition traces by MK-801
1492 (100 nM), an open channel pore blocker, of unlabeled (- MASp, black) and labeled (+ MASp,
1493 grey) GluN1/GluN2B WT NMDARs kept in the dark (MASp in its *trans* state). **(f)**
1494 Superposition of the normalized MK801 inhibition traces from Panel (e). Note the increase of
1495 MK-801 inhibition rate after labeling with MASp, indicating an increase in the open probability
1496 when GluN1/GluN2B NMDARs are conjugated with MASp. **(g)** Left, neutralization of the
1497 reactivity of C395, a cysteine located in GluN2B NTD-ABD linker, by mutation into a serine.
1498 Right, superposed and normalized MK-801 inhibition traces for labeled (+ MASp, grey) and
1499 unlabeled (- MASp, black) GluN1/GluN2B-C395S mutants. Note that on this mutant, labeling
1500 does not affect the rate of inhibition by MK-801. **(h)** Summary of the rates of inhibition by MK-
1501 801. n.s., $p > 0.05$; *, $p < 0.05$; multiple Mann-Whitney tests, p-values were adjusted for
1502 multiple comparisons using Bonferroni correction. Only the pre-selected indicated
1503 comparisons were performed.

1504

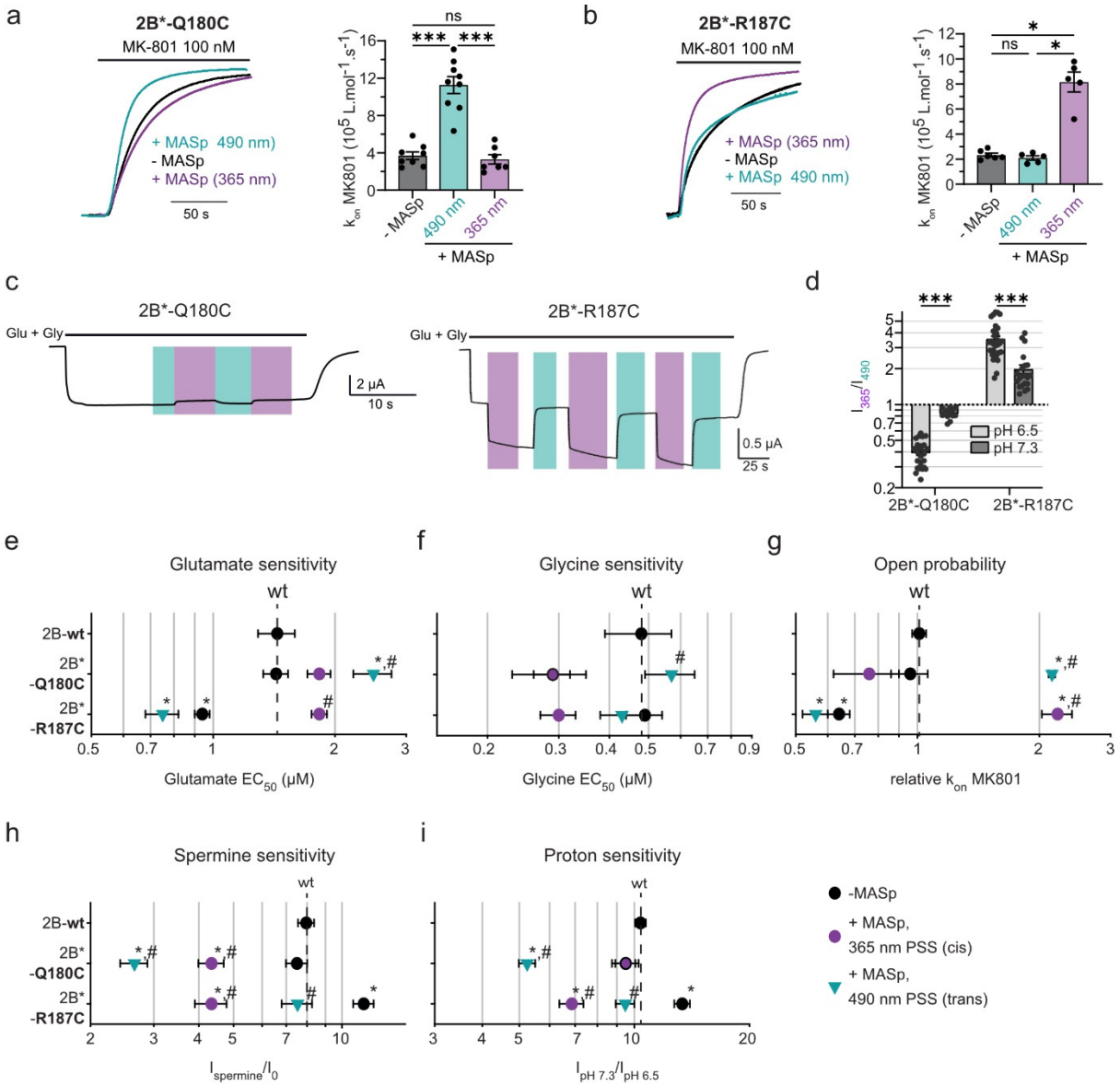

j

Criteria	Q180C	R187C
Photomodulation at physiological pH	1.2-fold	2-fold
cis-active photoswitch?	✗	✓
Functionally silent cys-teine mutation	✓	✓
Photoswitch inert in one configuration	✓	✓

Extended Data Fig. 2 (related to Fig. 1): Photomodulation and pharmacological properties of GluN2B*-Q180C and -R187C mutants.

(a,b) Evaluation of the relative Po of MASp-labeled GluN1/GluN2B*-Q180C (**a**) and GluN1/GluN2B*-R187C (**b**) under different light conditions. Left, superposed current traces following application of agonists and 100 nM MK-801 of unlabeled receptors (- MASp, black) and MASp-labeled receptors (+ MASp) under 365 (violet, mostly *cis*-MASP) or 490 nm light (blue-green, mostly *trans*-MASp). Right, summary of MK-801 inhibition rates. Kinetics of

1513 MK801 inhibition: 2B*-Q180C, k_{on} = 3.7 ± 0.4 10^5 $L.mol^{-1}.s^{-1}$, n = 8 (- MASp); 11.3 ± 0.9
1514 10^5 $L.mol^{-1}.s^{-1}$, n = 9 (+ MASp, 490 nm), and 3.3 ± 0.5 10^5 $L.mol^{-1}.s^{-1}$, n = 7 (+ MASp,
1515 365 nm); 2B*-R187C, k_{on} = 2.3 ± 0.1 10^5 $L.mol^{-1}.s^{-1}$, n = 6 (- MASp); 2.1 ± 0.2 10^5 $L.mol^{-1}.s^{-1}$,
1516 n = 5 (+ MASp, 490 nm), and 8.2 ± 1.6 10^5 $L.mol^{-1}.s^{-1}$, n = 5 (+ MASp, 365 nm). n.s., $p > 0.05$;
1517 *, $p < 0.05$; ***, $p < 0.001$; multiple Mann-Whitney test, p-values were adjusted for multiple
1518 comparisons using Bonferroni correction. When MASp was conjugated to GluN2B-Q180C in
1519 its *trans* configuration (under 490 nm light), channel Po increased by ~2-fold compared to
1520 unlabeled receptors, while labeling with *cis*-MASp (under UV light) produced no significant
1521 change in receptor activity. MASp thus acts as a *trans*-on photoswitch at position Q180C. In
1522 contrast, MASp conjugated to GluN2B-R187C had no effect on receptor channel Po under
1523 490 nm light, while it increased Po by ~3.5-fold under UV-light. MASp thus acts as a *cis*-on
1524 photoswitch at position R187C (see Fig. 1e, right). **(c,d)** Photomodulation of MASp-labeled,
1525 GluN1/GluN2B*-Q180C and -R187C receptors at physiological pH. **(c)** Current traces from
1526 MASp-labeled GluN1/GluN2B*-Q180C (left) and GluN1/GluN2B*-R187C (right) at pH 7.3. **(d)**
1527 Summary of photomodulation ratios for the Q180C and R187C mutants at pH 6.5 and 7.3.
1528 Photomodulation values at pH 6.5 are from Fig. 1. ***, $p < 0.001$ multiple Mann-Whitney
1529 tests, p-values were adjusted for multiple comparisons using Bonferroni correction. Only the
1530 pre-selected indicated comparisons were performed. Photomodulation values and number of
1531 cells are summarized in Supplementary Table 1. **(e-i)** Determination of the relative open
1532 probability and sensitivity to different pharmacological agents of unlabeled (- MASp) and
1533 labeled (+ MASp) GluN1/GluN2B*-Q180C and GluN1/GluN2B*-R187C receptors compared
1534 to unlabeled WT GluN1/GluN2B receptors. *, $p < 0.05$ between the condition and unlabeled
1535 WT GluN1/GluN2B receptors; #, $p < 0.05$, between MASp-labeled mutant receptors under
1536 365 or 490 nm light and unlabeled mutant receptors. One way Anova followed by Tukey's
1537 test. **(j)** Pros and cons of photo-enhancing GluN2B-NMDARs via the Q180C or the R187C
1538 labeling position. The R187C is the most favored labeling position due to its strong
1539 photomodulation at physiological pH and the fact that MASp at this position is active in *cis*.

1540

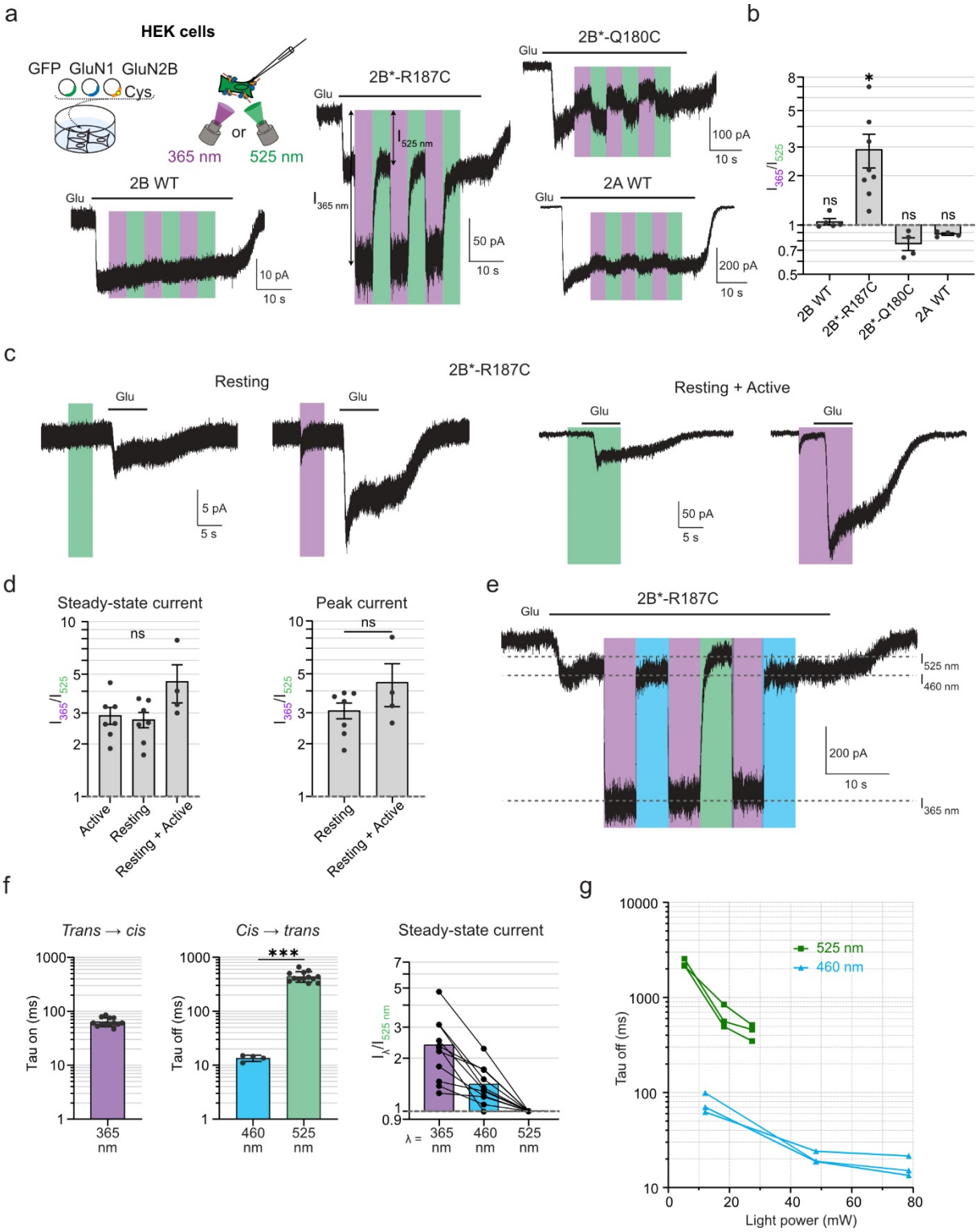

Extended Data Fig. 3 (related to Fig. 2): Up to 3-fold potentiation of GluN2B diheteromer currents in HEK cells.

(a) Current traces from MASp-labeled HEK cells expressing GluN1/GluN2B WT, GluN1/GluN2B*-Q180C, GluN1/GluN2B*-R187C, and GluN1/GluN2A WT receptors, following application of glutamate (100 µM) under 365 nm (violet bars) or 525 nm (green

1547 bars) illumination. Cells were constantly perfused with glycine (100 μM). **(b)** Summary of the
1548 photomodulation ratios ($I_{365\ nm}$ / $I_{525\ nm}$) of currents from the different receptors in (a)
1549 expressed in HEK cells. n.s., $p > 0.05$; **, $p < 0.01$; multiple one sample Wilcoxon tests
1550 against the value 1, p-values were adjusted for multiple comparisons using Bonferroni
1551 correction. Photomodulation values and number of cells are indicated in Supplementary
1552 Table 1. **(c,d)** No state-dependence of MASp-induced photomodulation. **(c)** GluN1/GluN2B*-
1553 R187C current traces in HEK cells under different illumination protocols. Left, light was
1554 applied before agonist application, allowing receptor modulation only from its resting state
1555 (Resting). Right, light was applied before and during agonist application, allowing receptor
1556 modulation from both its resting and activated states (Resting + Active). The small current
1557 peak observed at the onset of UV light in absence of agonist application corresponds to a
1558 transient potentiation of NMDARs tonically activated by small amounts of contaminating
1559 glutamate (see Extended Data Fig. 7). **(d)** Photomodulation ratios of steady-state (left) and
1560 peak (right) currents following light application during the active state only (Active, panel a),
1561 the resting state only (Resting, panel c, left) and both the active and resting states (resting +
1562 Active, panel c, right). Photomodulation ratios under these three states were measured from
1563 HEK cells from the same coverslip (hence labeled at the same time) to minimize any
1564 variability linked to the labeling procedure. n.s., $p > 0.05$, Kruskall Wallis (left) and Mann
1565 Whitney (right) tests. **(e-g)** Wavelength-dependence of MASp-induced photomodulation. **(e)**
1566 GluN1/GluN2B*-R187C current trace in a MASp-labeled HEK cell following illumination with
1567 UV (365 nm, violet bar), blue (460 nm, blue bar) or green (525 nm, green bar) light. Cells
1568 were pre-illuminated with blue light before current recording. **(f)** Time constants of current
1569 potentiation by UV light (left) and current recovery from potentiation by blue or green light
1570 (middle), and steady-state currents under the different light conditions relative to the current
1571 under green light, which represents the receptor basal activated state (right). Kinetics of
1572 photomodulation were measured at maximal light power through a 10x objective (~10 mW for
1573 365 nm, 79 mW for 460 nm and 27 mW for 525 nm). Tau on (365 nm) = 64 ± 13 ms (n = 13),
1574 Tau off (460 nm) = 13.5 ± 0.9 ms (n = 4), Tau off (525 nm) = 442 ± 27 ms (n = 13). ***,
1575 $p < 0.001$, Mann Whitney test. Relative steady-state (SS) values: SS(365 nm) = 2.38 ± 0.30;
1576 SS(460 nm) = 1.43 ± 0.11. **(g)** Kinetics of current recovery from potentiation by blue or green
1577 light as a function of light power. Recordings in HEK cells were performed at pH 7.3, -60 mV.

1578

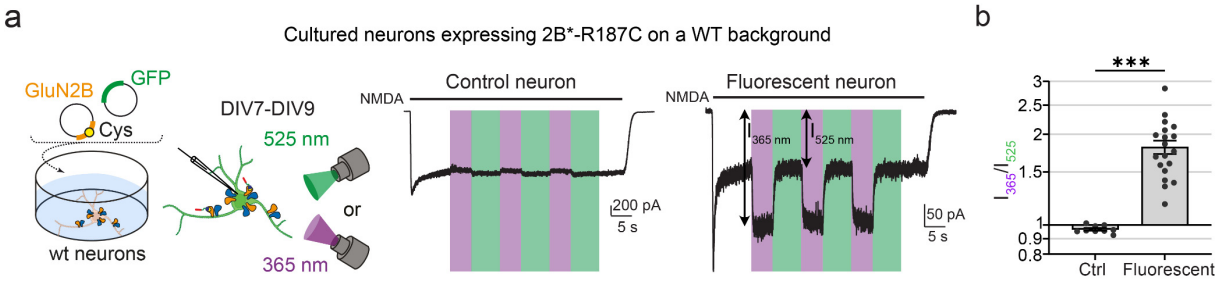

Extended Data Figure 4 (related to Fig. 2): Strong photomodulation of GluN2B*-R187C diheteromers in cultured cortical neurons.

(a) Left, expression of the GluN2B*-R187C subunit in cultured cortical neurons from wild-type animals through *ex utero* electroporation (see Methods). Right, current traces from DIV7-9 neurons labeled with MASp, following application of the selective NMDAR agonist NMDA (300 μM), under 365 nm (violet bars) or 525 nm (green bars) illumination. Cells were constantly perfused with D-serine (50 μM). Fluorescent neurons express the 2B*-R187C subunit, while non-fluorescent (control) neurons only express the endogenous NMDAR population. (**b**) Summary of photomodulation ratios of MASp-labeled, fluorescent and control (non-fluorescent) neurons. ***, $p < 0.001$, Mann Whitney test. Recordings in cultured cortical neurons were performed at pH 7.3, -60 mV. Photomodulation values and number of cells are summarized in Supplementary Table 1.

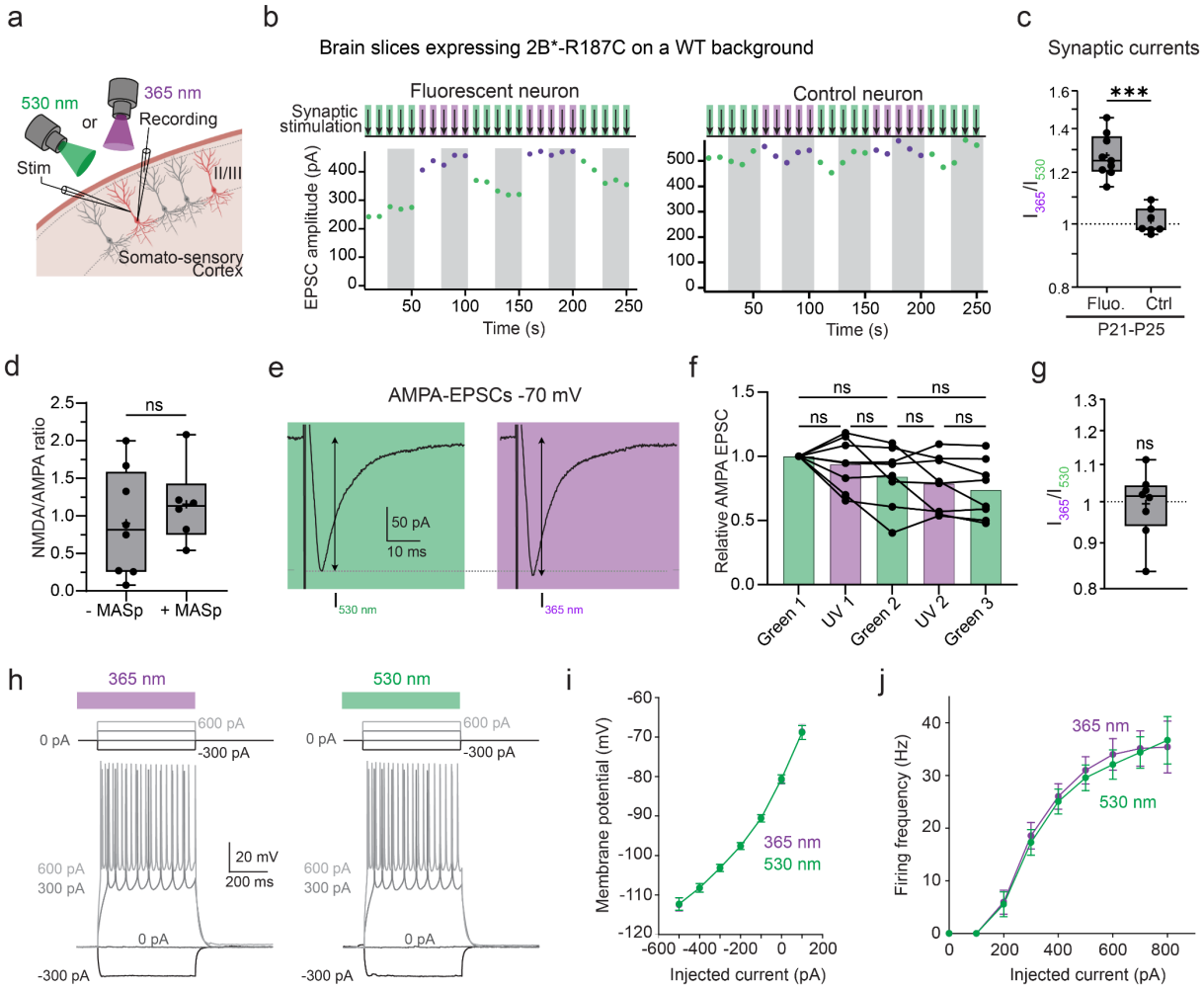

Extended Data Fig. 5 (related to Fig. 3): Protocol of photomodulation of NMDA-EPSCs and determination of MASp background effects on brain slices.

(a) Data were obtained from electroporated (fluorescent) and non-electroporated (non fluorescent, control) layer II/II pyramidal neurons from the somatosensory cortex upon stimulation at the level of their apical dendrite. **(b)** Top, protocol of photomodulation of NMDAR synaptic currents (NMDA-EPSCs). Synaptic stimulation was performed continuously at 0.1 Hz. 525 nm (green bars) or 365 nm (violet bars) illumination started 1 s before synaptic stimulation and ended 200 ms after synaptic stimulation (1.2 s total). Illumination cycles consisted of alternations between 5 stimulations under 525 nm light and 5 stimulations under 365 nm light. Bottom, amplitudes of NMDAR-EPSCs from a MASp-labeled, fluorescent (expressing GluN2B*-R187C) neuron from a P14 mouse under alternating 525 nm (green points) and 365 nm (violet points) illumination, showing reversible and reproducible photomodulation of NMDA-EPSCs. Given the slow reversion of EPSC amplitude by 525 nm light, only the three last EPSCs of each 5-stimulation cycle were considered for amplitude quantification and trace averaging (grey bars). **(c)** Photomodulation ratios ($I_{365\ nm}$ / $I_{525\ nm}$) of NMDA-EPSCs of MASp-labeled, fluorescent and control neurons from P21-P25 animals.

1610 Photomodulation values and number of cells are summarized in Supplementary Table 3**. (d-j)**
1611 MASp labeling has no or minimal impact on synaptic transmission and neuronal electrical
1612 properties **(d)** NMDA/AMPA ratios for WT neurons either unlabeled (- MASp, n = 8) or labeled
1613 (+ MASp, n = 6) from P21-P25 animals. n.s., $p > 0.05$, Mann Whitney test. **(e-g)** No
1614 photodependent effect of MASp labeling on AMPA-EPSCs. **(e)** Representative AMPA-EPSCs
1615 (recorded at -70 mV) from a MASp-labeled control (non-fluorescent) layer II/III cortical
1616 neuron under 525 nm (green bar, left) or 365 nm light (violet bar, right) in a slice from a P21
1617 mouse. Same illumination conditions as in Panel b. **(f)** Summary of AMPA-EPSC amplitudes
1618 of MASp-labeled control neurons from P21-P22 mice under alternating 525 nm (green bars)
1619 and 365 nm (violet bars) illumination. Each dot represents the average amplitude of AMPA-
1620 EPSCs for each cycle for each cell. n.s., $p > 0.05$; Repeated measures Anova followed by
1621 Tukey's multiple comparison test. **(g)** Photomodulation ratios of AMPA-EPSCs from MASp-
1622 labeled, control neurons, showing no significant photomodulation. Quantification of the
1623 photomodulation ratio was performed similarly to Fig. 3. n.s., $p > 0.05$; one sample Wilcoxon
1624 test against the value of 1. **(h-j)** No photodependence of the excitability properties of MASp-
1625 labeled control neurons. **(h)** Current-clamp voltage traces of a MASp-labeled, control neuron
1626 from a P23 mouse during 500 ms current injection steps under UV (365 nm, violet bar) and
1627 green light (525 nm, green bar). UV light was applied 50 ms before and during the current
1628 step, while green light was applied 2 s before and during the current step. The amount of
1629 current injected is written next to the corresponding voltage trace. **(i,j)** No light-dependence
1630 of the membrane potential (i) and firing frequency (j) as a function of injected current after
1631 MASp labeling of control neurons from P21-P24 animals. All recordings in brain slices were
1632 performed at physiological pH.

1633

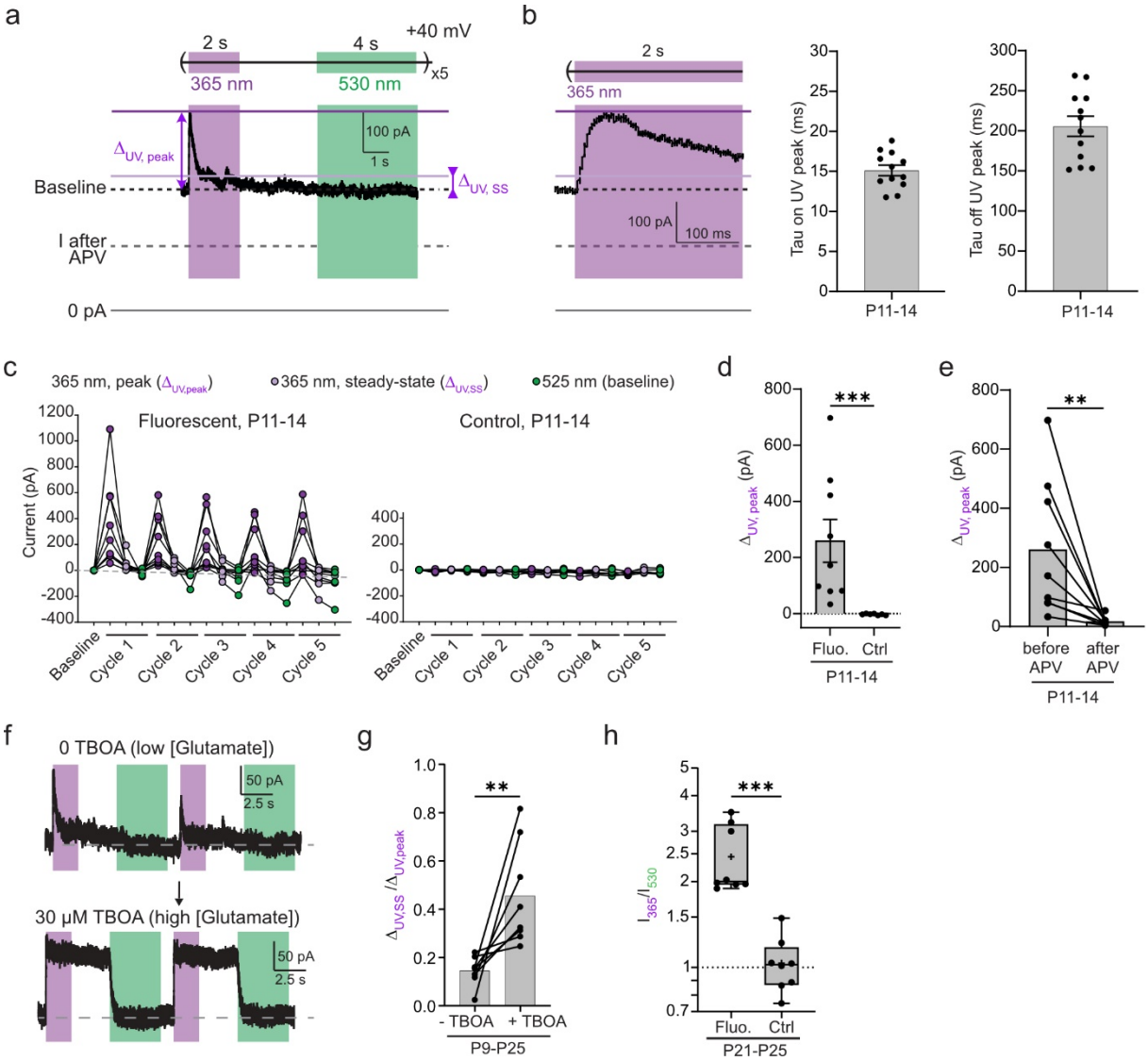

Extended Data Fig. 6 (related to Fig. 3):

Unless otherwise noted, experiments were performed on slices from P11-14 electroporated animals. **(a)** NMDAR tonic current trace of the MASp-labeled, P13 fluorescent neuron shown in Fig. 3d displaying the different values used in the following panels. $\Delta_{UV,\ peak}$ represents the difference between the peak current amplitude at the onset of UV irradiation and the current amplitude under green light (baseline current). $\Delta_{UV,\ SS}$ represents the difference between the steady-state current amplitude at the end of UV irradiation and the current amplitude under green light (baseline current). **(b)** Left, zoom on the UV-induced peak of the NMDA tonic current trace from (a). Middle and right, time constants of UV-induced potentiation (Tau on UV peak, left) and relaxation (Tau off UV peak, right). Tau on UV peak = 15.1 ± 0.7 ms, n = 12 and Tau off UV peak = 206 ± 13 ms, n = 12. **(c)** Tonic current amplitudes of MASp-labeled, fluorescent (left) and control (right) neurons during the 5-cycle illumination protocol. See Panel (a) for annotations. **(d)** UV-induced increase of tonic current amplitude at peak ($\Delta_{UV,\ peak}$) for each MASp-labeled, fluorescent and control (non-fluorescent, denoted ctrl)

1649 neuron displayed in Panel c, and averaged over the 5 cycles of illumination. ***, $p < 0.001$,
1650 Mann Whitney test. **(e)** APV suppresses UV-induced increase of tonic current at peak of
1651 MASp-labeled, fluorescent neurons. **, $p < 0.01$, Mann-Whitney test. **(f)** Photomodulation of
1652 the tonic current of a MASp-labeled, P9 fluorescent neuron in basal conditions (0 TBOA, top)
1653 and after 10 min treatment of the slice with the glutamate transporter inhibitor TBOA (30 μM
1654 TBOA, bottom). As tonic glutamate concentration increases, UV-induced potentiation goes
1655 from transient to sustained. **(g)** Relative amplitude of steady-state over peak UV-induced
1656 increase in tonic current ($\Delta_{UV, SS}$ / $\Delta_{UV, peak}$) before (-TBOA) and after (+TBOA) TBOA
1657 treatment. Animals with ages ranging from P9 to P25 were used for this experiment. **,
1658 $p < 0.01$; Wilcoxon matched-pairs signed rank test. **(h)** Photomodulation ratios of NMDA tonic
1659 currents of MASp-labeled, fluorescent and control (non-fluorescent) neurons from P21-P25
1660 animals. Photomodulation values and cell numbers are summarized in Supplementary
1661 Table 3. ***, $p < 0.001$, Mann Whitney test. All recordings in brain slices were performed at
1662 physiological pH.

1663

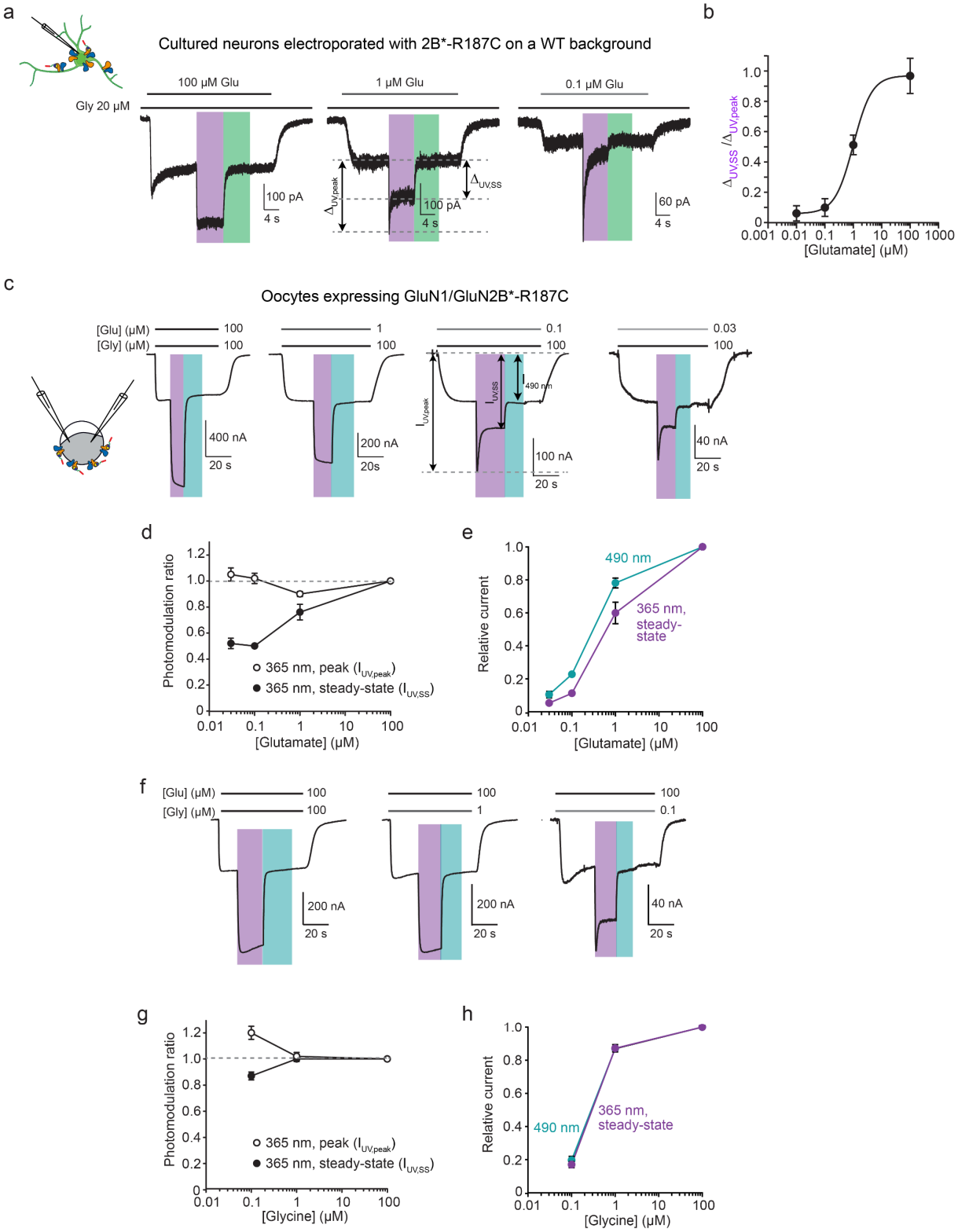

Extended Data Fig. 7 (related to Fig. 3): Stability of Opto2B photoenhancement depends on glutamate concentration.

(a) Current traces from a cultured cortical neuron electroporated with the GluN2B*-R187C subunit and labeled with MASp showing transient UV (violet bar)-induced potentiation of NMDAR currents under non-saturating glutamate (Glu) concentrations (0.1 and 1 μM), while

1670 UV potentiation was stable at saturating glutamate concentration (100 μM). NMDAR currents
1671 were isolated using 10 μM NBQX, 100 μM picrotoxin and 10 μM strychnine, and 20 μM
1672 glycine was applied throughout the experiment (same conditions as in *ex vivo* experiments in
1673 Fig. 3). The experimental strategy to express the mutated GluN2B subunit on a WT
1674 background was the same as in Extended Data Fig. 4a. **(b)** The ratio of steady-state over
1675 peak current ($\Delta_{UV, SS}$ / $\Delta_{UV, peak}$; see Panel (a) for measurement of $\Delta_{UV, SS}$ and $\Delta_{UV, peak}$)
1676 increases as glutamate concentration increases. Recordings were performed at pH 7.3, -
1677 60 mV. **(c-h)** Experiments were performed in Xenopus oocytes expressing GluN1/GluN2B*-
1678 R187C at pH 6.5, -60 mV. **(c-e)** Glutamate dependence of GluN2B diheteromer
1679 photomodulation. **(c)** Current traces from an oocyte expressing GluN1/GluN2B*-R187C and
1680 labeled with MASp following application of varying concentrations of glutamate together with
1681 a saturating concentration (100 μM) of glycine and under 365 (violet bar) or 490 nm (blue-
1682 green bar) illumination. **(d)** While the photomodulation ratios at steady-state ($I_{UV, SS}$ / $I_{490\ nm}$,
1683 black dots) are highly dependent on glutamate concentration, the photomodulation ratios
1684 calculated from the UV peak currents ($I_{UV, peak}$ / $I_{490\ nm}$, white dots) were almost independent of
1685 glutamate concentration (they varied by less than 10% across all glutamate concentrations).
1686 For each cell, $I_{UV, peak}$ was measured at the time of peak measured for 0.1 μM glutamate, i.e.
1687 ~0.9 s after the onset of UV illumination. $I_{UV, SS}$ was measured at the end of the UV
1688 illumination step. $I_{490\ nm}$ was measured at the end of the 490 nm illumination step. **(e)** Relative
1689 currents at different glutamate concentrations normalized to the current at 100 μM glutamate
1690 (saturating concentration). **(f-h)** Glycine dependence of GluN1/GluN2B photomodulation. **(f)**
1691 Current traces from an oocyte expressing GluN1/GluN2B*-R187C and labeled with MASp
1692 following application of varying concentrations of glycine together with a saturating
1693 concentration (100 μM) of glutamate and under 365 (violet bar) or 490 nm (blue-green bar)
1694 illumination. **(g)** UV potentiation was stable for 100 and 1 μM glycine but became transient
1695 for 0.1 μM glycine. Maximum UV potentiation ($I_{UV, peak}$ / $I_{490\ nm}$, white dots) increased by 20% at
1696 low glycine concentrations compared to higher 1 and 100 μM concentrations. **(h)** Relative
1697 currents at different glycine concentrations normalized to the current at 100 μM glycine
1698 (saturating concentration).

1699

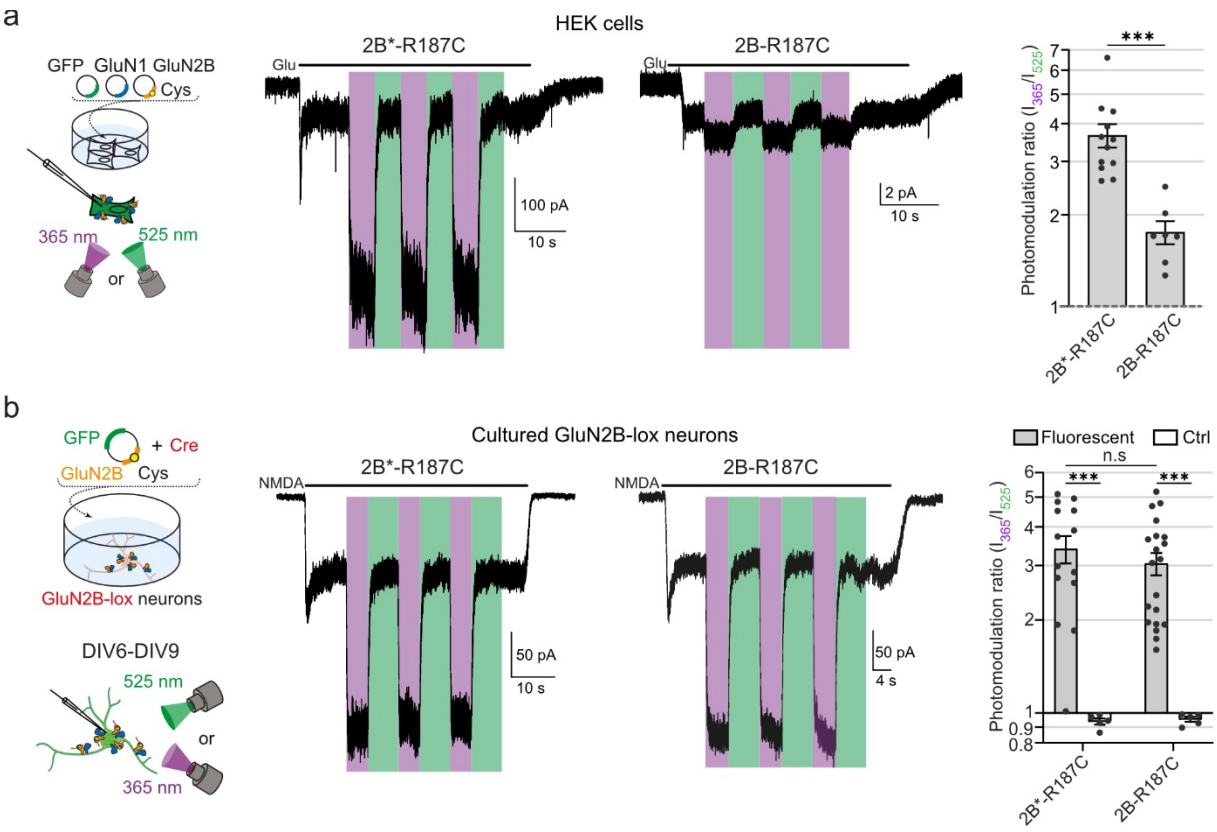

Extended Data Fig. 8 (related to Fig. 4): Design strategy of the Opto2B mouse line: neutralizing the endogenous cysteine C395 is not necessary to obtain strong photomodulation in native preparations.

(a) Left, current traces from HEK cells expressing GluN1/GluN2B-R187C-C395S (GluN1/GluN2B*-R187C) and GluN1/GluN2B-R187C receptors (with endogenous cysteine 395 intact), and labeled with MASp, following application of glutamate (100 µM) under 365 nm (violet bars) or 525 nm (green bars) illumination. Cells were constantly perfused with glycine (100 µM). Right, summary of the photomodulation ratios ($I_{365\ nm}$ / $I_{525\ nm}$) for the different GluN2B mutants expressed in HEK cells. Note that the photomodulation ratio is much lower for GluN1/GluN2B-R187C (1.75 ± 0.15, n = 7) compared to GluN1/GluN2B*-R187C (3.66 ± 0.32, n = 12). ***, $p < 0.001$; Mann Whitney test. **(b)** Left, current traces from DIV6-9 cortical neurons expressing GluN1/GluN2B-R187C-C395S (GluN1/GluN2B*-R187C) and GluN1/GluN2B-R187C receptors, and labeled with MASp, following application of NMDA (300 µM) under 365 nm (violet bars) or 525 nm (green bars) illumination. Cells were constantly perfused with D-serine (50 µM). In this particular experiment, we adopted a strategy of molecular replacement of the endogenous, WT GluN2B subunits by the mutated GluN2B subunits using the Cre-lox approach. Dissociated cortical neurons from floxed-Grin2B mice[100] were electroporated with pIRES plasmids coding for GFP and a mutated GluN2B subunit[23], and plasmids coding for the Cre recombinase (to remove endogenous

1720 GluN2B expression) and for the fluorescent marker TdTomato (see Methods). Right,
1721 summary of the photomodulation ratios ($I_{365\ nm}$ / $I_{525\ nm}$) of currents from the different GluN2B
1722 mutants expressed in cultured neurons. Note that, contrary to what was observed on HEK
1723 cells, the photomodulation ratio is similar between GluN1/GluN2B-R187C (3.04 ± 0.25,
1724 n = 20) and GluN1/GluN2B*-R187C (3.25 ± 0.35, n = 15). n.s, $p > 0.05$; ***, $p < 0.001$;
1725 Multiple Mann-Whitney tests, p-values were adjusted for multiple comparisons using
1726 Bonferroni correction. Only the pre-selected indicated comparisons were performed. All
1727 recordings were performed at pH 7.3, -60 mV.

1728

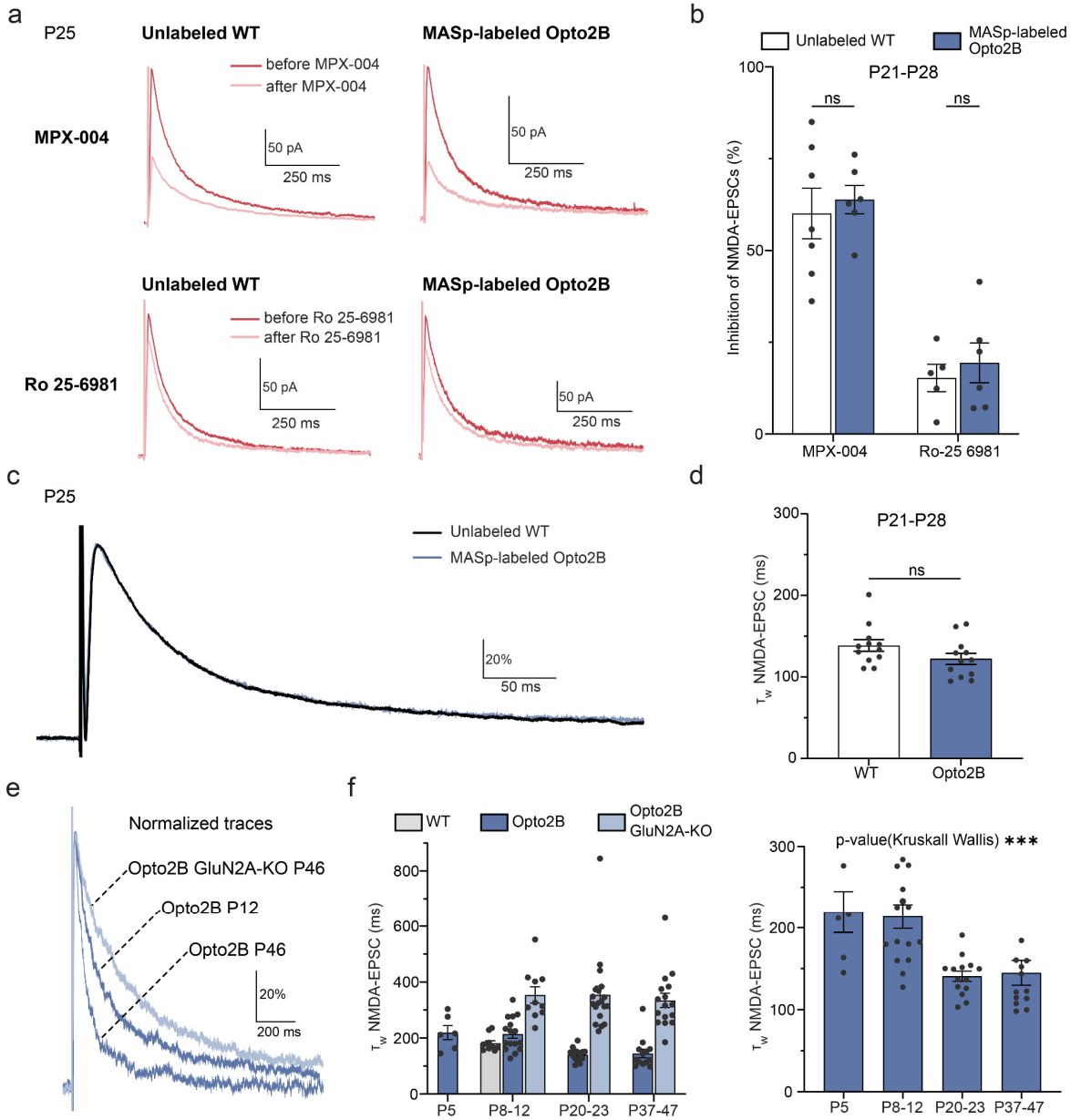

Extended Data Fig. 9 (related to Fig. 4): Similar NMDAR subunit profiles between Opto2B and WT mice.

(a) Top, superposition of NMDA-EPSCs of CA1 pyramidal neurons before and after application of MPX-004 (top) or Ro 25-6981 (bottom) from unlabeled WT (left) and MASp-labeled Opto2B mice (right) at age P25, recorded in the dark (MASp in its inactive, *trans* configuration). **(b)** Summary of NMDA-EPSC inhibition (%) by MPX-004 or Ro 25-6981 of CA1 pyramidal neurons from unlabeled WT (white) and MASp-labeled Opto2B mice (blue) at P21-P28. n.s., $p > 0.05$; multiple Mann-Whitney tests, p-values were adjusted using Bonferroni correction. Only the pre-selected indicated comparisons were performed. **(c)** Superposition of normalized NMDA-EPSCs of CA1 pyramidal neurons from unlabeled WT

1740 (black) and MASp-labeled Opto2B mice (blue) at age P25. **(d)** Summary of NMDA-EPSC
1741 decay kinetics from unlabeled WT (white) and MASp-labeled Opto2B mice (blue) at P21-P28.
1742 n.s., $p > 0.05$; Mann Whitney test. Note the similar NMDA-EPSC decay time between WT
1743 and Opto2B animals, suggesting that the R187C mutation does not perturb developmental
1744 maturation of NMDA subtypes. **(e)** Superposition of normalized NMDA EPSCs of MASp-
1745 labeled CA1 pyramidal neurons from Opto2B mice at age P12 and P46, as well as from P46
1746 Opto2B/GluN2A KO animals, recorded under green light (MASp in its inactive configuration).
1747 Each trace is the average of 12 individual EPSCs. **(f)** Left, decay time constants (τ_w NMDA-
1748 EPSC) of NMDA-EPSCs of MASp-labeled CA1 pyramidal neurons from WT (grey), Opto2B
1749 (dark blue) and Opto2B GluN2A-KO (light blue) mice at different age ranges. Note the
1750 absence of significant difference between the NMDA-EPSC decay kinetics of from WT and
1751 Opto2B animals at P8-P12, suggesting similar NMDAR subunit populations. NMDA-EPSC
1752 decay kinetics from Opto2B/GluN2A KO mice remained slow at older ages, consistently with
1753 what was previously shown for animals lacking GluN2A expression[81]. Right, zoom on the
1754 Opto2B mouse condition for better visualization. ***, $p < 0.001$, Kruskall-Wallis test on
1755 Opto2B condition. Note the acceleration of NMDA-EPSC decay time with age on Opto2B
1756 mice, which is consistent with what was observed in the literature on WT animals[16]. All the
1757 recordings on brain slices were performed at physiological pH.

1758

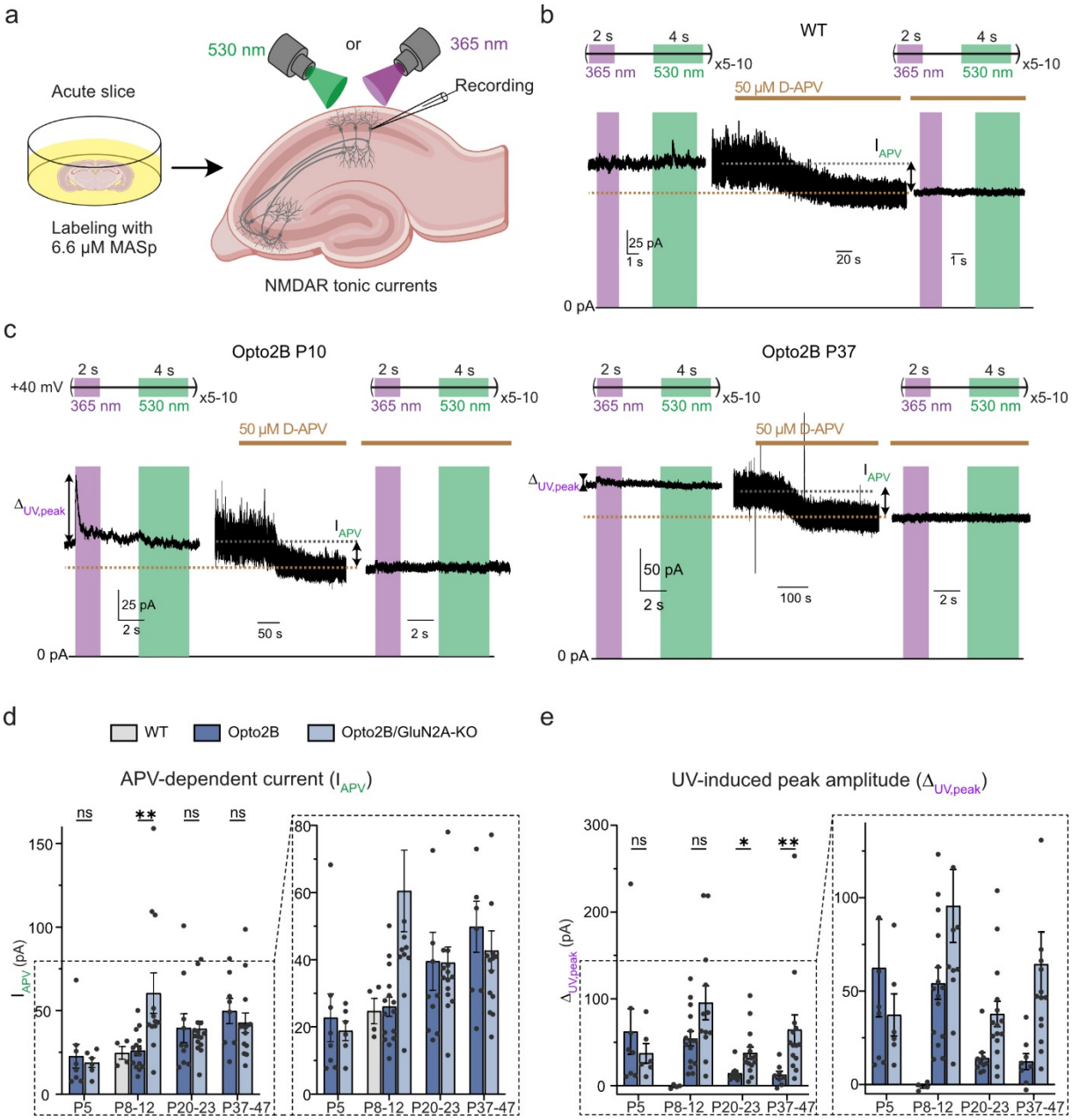

Extended Data Fig. 10 (related to Fig. 5):

(a) Protocol of tonic current photomodulation. Note the absence of electrical stimulation: recorded tonic currents are mediated by low levels of tonic glutamate. See Methods and Main Text for more details. **(b)** Tonic current trace of a MASp-labeled, CA1 pyramidal neuron from a P10 WT mouse before (left) and during (middle and right) application of 50 µM D-APV. Left and right traces are the average of 5 to 10 traces. Note the absence of photomodulation. **(c)** Tonic current traces of MASp-labeled, CA1 pyramidal neurons from a P10 (left) or a P37 (right) Opto2B mouse before and during application of 50 µM D-APV. Left and right traces are the average of 5 to 10 traces. Displayed arrows indicate the currents measured in the following panels and used to calculate the photomodulation ratio (see also Fig. 3). **(d)** Amplitude of APV-sensitive currents (as shown in a) of MASp-labeled, CA1 pyramidal

1771 neurons from WT (grey), Opto2B (dark blue) and Opto2B GluN2A-KO (light blue) mice
1772 according to age ranges. Right, zoom on data for better visibility of bar graphs. **(e)** Amplitude
1773 of the UV-induced peak (as shown in a) of MASp-labeled, CA1 pyramidal neurons from WT
1774 (grey), Opto2B (dark blue) and Opto2B GluN2A-KO (light blue) mice according to age
1775 ranges. Right, zoom on data for better visibility of bar graphs. All recordings in brain slices
1776 were performed at physiological pH.

1777